ACCEPTED TO APJ
Preprint typeset using LaTeX style emulateapj v. 5/2/11

THE MOSDEF SURVEY: DYNAMICAL AND BARYONIC MASSES AND KINEMATIC STRUCTURES OF STAR-FORMING GALAXIES AT $1.4 \leq z \leq 2.6$

SEDONA H. PRICE[1], MARISKA KRIEK[1], ALICE E. SHAPLEY[2], NAVEEN A. REDDY[3,5], WILLIAM R. FREEMAN[3], ALISON L. COIL[4], LAURA DE GROOT[3], IRENE SHIVAEI[3], BRIAN SIANA[3], MOJEGAN AZADI[4], GUILLERMO BARRO[1], BAHRAM MOBASHER[3], RYAN L. SANDERS[2], AND TOM ZICK[1]

Accepted to ApJ

ABSTRACT

We present Hα gas kinematics for 178 star-forming galaxies at $z \sim 2$ from the MOSFIRE Deep Evolution Field survey. We have developed models to interpret the kinematic measurements from fixed-angle multi-object spectroscopy, using structural parameters derived from CANDELS *HST*/F160W imaging. For 35 galaxies we measure resolved rotation with a median $(V/\sigma_{V,0})_{R_E} = 2.1$. We derive dynamical masses from the kinematics and sizes and compare them to baryonic masses, with gas masses estimated from dust-corrected Hα star formation rates (SFRs) and the Kennicutt-Schmidt relation. When assuming that galaxies with and without observed rotation have the same median $(V/\sigma_{V,0})_{R_E}$, we find good agreement between the dynamical and baryonic masses, with a scatter of $\sigma_{\rm RMS} = 0.34\,{\rm dex}$ and a median offset of $\Delta \log_{10} M = 0.04\,{\rm dex}$. This comparison implies a low dark matter fraction (8% within an effective radius) for a Chabrier initial mass function (IMF), and disfavors a Salpeter IMF. Moreover, the requirement that $M_{\rm dyn}/M_{\rm baryon}$ should be independent of inclination yields a median value of $(V/\sigma_{V,0})_{R_E} = 2.1$ for galaxies without observed rotation. If instead we treat the galaxies without detected rotation as early-type galaxies, the masses are also in reasonable agreement ($\Delta \log_{10} M = -0.07\,{\rm dex}$, $\sigma_{\rm RMS} = 0.37\,{\rm dex}$). The inclusion of gas masses is critical in this comparison; if gas masses are excluded there is an increasing trend of $M_{\rm dyn}/M_*$ with higher specific SFR (SSFR). Furthermore, we find indications that V/σ decreases with increasing Hα SSFR for our full sample, which may reflect disk settling. We also study the Tully-Fisher relation and find that at fixed stellar mass $S_{0.5} = \left(0.5V_{2.2}^2 + \sigma_{V,0}^2\right)^{1/2}$ was higher at earlier times. At fixed baryonic mass, we observe the opposite trend. Finally, the baryonic and dynamical masses of the active galactic nuclei in our sample are also in excellent agreement, suggesting that the kinematics trace the host galaxies.

Subject headings: galaxies: kinematics and dynamics — galaxies: evolution — galaxies: high-redshift

1. INTRODUCTION

In the local universe, most massive star-forming galaxies have traditional Hubble-type morphologies and relatively smooth and thin stellar disks (e.g., Blanton & Moustakas 2009). These disks are thought to form from the cooling of baryons within dark matter halos (White & Rees 1978, Fall & Efstathiou 1980, Blumenthal et al. 1984, White & Frenk 1991). Galaxy formation models (both semi-analytic models, e.g. Dalcanton et al. 1997; Mo et al. 1998, and hydrodynamic simulations, e.g. van den Bosch 2001; Governato et al. 2007; Dutton 2009) are able to reproduce realistic local disk galaxies. However, testing these specific models requires direct observations of galaxies throughout cosmic time.

Over the past two decades, technological advances have enabled observations that provide new insights into the nature of star-forming galaxies at intermediate and high redshifts, in particular due to the combination of high-resolution multi-wavelength imaging with the *Hubble Space Telescope* (*HST*) and near-infrared integral-field spectroscopy with ground-based telescopes. The kinematics and structures of star-forming galaxies have been measured out to $z \sim 2$ (e.g., Weiner et al. 2006, Kassin et al. 2007, 2012, Noeske et al. 2007, Miller et al. 2011, 2012, 2013, Szomoru et al. 2011, Contini et al. 2012, Nelson et al. 2012, 2013, 2015, van Dokkum et al. 2013, Buitrago et al. 2014), the epoch during which the star formation rate (SFR) density in the universe is at its peak value. At this time, massive star-forming galaxies generally look very different from similar-mass star-forming galaxies today (e.g., Fan et al. 2001, Chapman et al. 2005, Hopkins & Beacom 2006, Reddy & Steidel 2009). They tend to be smaller (e.g., Williams et al. 2010, van der Wel et al. 2014a), morphologically clumpier (e.g., Elmegreen & Elmegreen 2006, Elmegreen et al. 2007, 2009, Law et al. 2007b, 2009, 2012b, Genzel et al. 2008, Förster Schreiber et al. 2009, 2014), have thicker disks (Elmegreen & Elmegreen 2006), and higher gas fractions (Daddi et al. 2008, 2010, Tacconi et al. 2008, 2010, 2013, Swinbank et al. 2011).

Many massive star-forming galaxies at $z \sim 2$ do have rotating disks – similar to their local counterparts – but tend to have higher velocity dispersions (and therefore lower V/σ, i.e. the ratio of rotation to velocity dispersion) than local star-forming galaxies (e.g., Epinat et al. 2008, 2010, Green et al. 2014). The higher velocity dispersions at higher redshifts are thought to reflect increased turbulence and thickened disks (e.g., Förster Schreiber et al. 2006, 2009, Wright et al. 2007, 2009, Genzel et al. 2008, 2011, Law et al. 2007a, 2009, 2012a, Wisnioski et al. 2012, 2015, Newman et al. 2013). Theoretical models suggest that the higher turbulence and clumpier morphology of massive star-forming galaxies at $z \sim 2$ rela-

[1] Department of Astronomy, University of California, Berkeley, CA 94720, USA; sedona@berkeley.edu
[2] Department of Physics & Astronomy, University of California, Los Angeles, CA 90095, USA
[3] Department of Physics & Astronomy, University of California, Riverside, CA 92521, USA
[4] Center for Astrophysics and Space Sciences, University of California, San Diego, La Jolla, CA 92093, USA
[5] Alfred P. Sloan Fellow

tive to their local counterparts are the result of the higher gas fractions (e.g., Dekel et al. 2009, Bournaud et al. 2011, Genel et al. 2012), and that the gas-rich, thicker disks are built-up by smooth, cold-mode gas accretion or minor mergers (e.g., Kereš et al. 2005, 2009, Dekel & Birnboim 2006, Davé 2008, Dekel et al. 2009, Oser et al. 2010, Cacciato et al. 2012, Ceverino et al. 2012).

However, the theoretical interpretation of the structures of distant star-forming galaxies is complicated by observational limitations, including low spatial resolution and small sample sizes. For example, initial studies with SINFONI found that one third (14 of 47) of star-forming galaxies at $z \sim 2$ appeared to be small and dispersion dominated (i.e., $V/\sigma < 1$; Förster Schreiber et al. 2009). Nonetheless, Newman et al. (2013) revealed that objects that do not show evidence for rotation in the lower resolution observations, especially objects with sizes close to the previous resolution limit, do show evidence for rotation in follow-up adaptive-optics assisted IFU observations. Thus, small rotationally-supported galaxies may appear to be dispersion dominated because of smearing caused by resolution limitations.

New near-infrared (NIR) spectrographs, including KMOS (Sharples et al. 2004, 2013) and MOSFIRE (McLean et al. 2010, 2012) have multiplexing capabilities, and thus allow for extensive kinematic studies of large, complete samples of galaxies at $z \sim 2$. However, as both KMOS and MOSFIRE are seeing limited, kinematic measurements of the majority of the star-forming galaxies at $z \sim 2$ with $\log_{10}(M_*/M_\odot) \lesssim 10$ will suffer from the same resolution problem as the seeing-limited SINFONI studies. Additionally, multi-slit spectrographs like MOSFIRE have no IFU and a constant position angle for all slits in one mask. The mask orientation is generally set by the algorithm to maximize the number of targets in a mask, and thus the slit position angle is randomly oriented compared to the galaxy major axes. The random slit orientations introduce additional challenges to interpreting the observed kinematic information.

Despite these complications, we can take advantage of the large galaxy surveys afforded by multi-object NIR spectrographs by combining these observations with high-resolution rest-frame optical imaging from *HST*. Ancillary *HST*/WFC3 data accurately show what portion of a galaxy falls within the slit, and can be used to interpret the observed spectrum. Furthermore, by using large galaxy samples with detailed ancillary measurements, we can apply statistical approaches to constrain the kinematic structures of galaxies. For example, van der Wel et al. (2014b) use the distribution of observed axis ratios to constrain the structures of star-forming galaxies.

In this paper we study the dynamical and baryonic masses and kinematic structures of a sample of 178 star-forming galaxies using data from the MOSFIRE Deep Evolution Field (MOSDEF) survey (Kriek et al. 2015). The galaxies are observed with random orientations between the slit and kinematic major axes, and rotation is detected in only 35 galaxies. However, for the galaxies without detected rotation we take advantage of our large sample size, accurate Hα SFRs, stellar masses and detailed morphological information from imaging of the CANDELS survey (Koekemoer et al. 2011, Grogin et al. 2011) to constrain their kinematics. We derive dynamical masses for all galaxies, compare them with baryonic masses, and discuss the implications for the structures of the galaxies, the stellar initial mass function (IMF) and dark matter fraction, and the gas kinematics of active galactic nuclei (AGN) host galaxies.

The paper is organized as follows. In Section 2, we present our sample and the ancillary measurements. The methods of extracting kinematic information from both 2D spectra and integrated 1D spectra are detailed in Section 3. In Section 4, we present the baryonic and dynamical masses, as well as V/σ, for both the galaxies with and without detected rotation. The implications and caveats of our results are presented in Section 5. We summarize our results in Section 6.

Throughout this paper we adopt a ΛCDM cosmology with $\Omega_m = 0.3$, $\Omega_\Lambda = 0.7$, and $H_0 = 70\ \mathrm{km\,s^{-1}\,Mpc^{-1}}$.

2. DATA

2.1. *The MOSDEF Survey*

We make use of data from the MOSDEF survey (Kriek et al. 2015), conducted using the MOSFIRE spectrograph (McLean et al. 2012) on the 10 m Keck I telescope. In this work, we use the spectra obtained during semesters 2012B, 2013A, and 2014A. When complete, the MOSDEF survey will contain moderate resolution ($R = 3000 - 3650$) rest-frame optical spectra for ~ 1500 H-band selected galaxies at $1.4 \leq z \leq 3.8$ in several Cosmic Assembly Near-Infrared Deep Extragalactic Legacy Survey (CANDELS; Koekemoer et al. 2011, Grogin et al. 2011) fields. A detailed overview of the survey, observations, data reduction, line measurements and sensitivities, success rate, redshift measurements, stellar population properties, and sample characteristics are given in Kriek et al. (2015).

For all galaxies observed with MOSFIRE, we measure structural parameters, including the Sérsic index, n (Sérsic 1968), the effective radius, R_E (assumed to be the semi-major axis, unless explicitly stated otherwise), the axis ratio, b/a, and the major axis position angle from the *HST*/F160W images (released by the CANDELS team) using GALFIT (Peng et al. 2010). See L. de Groot et al. (in preparation) for more details on the structural parameter measurements.

Stellar masses for all MOSDEF galaxies are derived by fitting the $0.3 - 8.0\,\mu$m photometry from the 3D-HST survey (Brammer et al. 2012, Skelton et al. 2014, Momcheva et al. 2015) with the flexible stellar population models (Conroy et al. 2009, Conroy & Gunn 2010) using FAST (Kriek et al. 2009), while adopting the MOSFIRE redshifts ($z_{\rm MOS}$). We assume a Chabrier (2003) stellar IMF, along with a Calzetti et al. (2000) dust attenuation curve, a delayed exponentially-declining star formation history, and solar metallicity. To account for template mismatch, we assume the default FAST template error function. Confidence intervals are calibrated using 500 Monte Carlo simulations. Hence, the stellar mass uncertainties do not include systematic uncertainties due to the choice of IMF, dust attenuation curve, or other assumptions. See Kriek et al. (2015) for more details on the stellar population modeling.

Following Taylor et al. (2010), we correct the stellar masses by the difference between the GALFIT ($m_{\rm GALFIT}$) and total photometric F160W magnitudes ($m_{\rm phot}$), using

$$\log_{10} M_* = \log_{10} M_{*,\,\rm FAST} + 0.4(m_{\rm phot} - m_{\rm GALFIT}). \quad (1)$$

This correction makes the size and stellar mass measurements self-consistent.

Emission line fluxes are measured from the optimally extracted MOSFIRE 1D spectra by fitting adjacent lines simultaneously with Gaussians plus a linear fit to account for the underlying continuum. The Hα and Hβ lines are corrected for the underlying Balmer absorption, as estimated from the

best-fit stellar population models. See Kriek et al. (2015) and Reddy et al. (2015) for more details on the emission line measurements.

We use the Hα emission lines to estimate SFRs and gas masses ($M_{\rm gas}$) using the following method. For galaxies with detected Hβ, the Balmer absorption-corrected Hα fluxes are corrected for dust using the Balmer decrement, assuming a Cardelli et al. (1989) extinction curve (Reddy et al. 2015). When Hβ is undetected, we assume the reddening of the nebular regions is related to that of the continuum by $A_{\rm V,neb,Calzetti} = 1.86\,A_{\rm V,cont,Calzetti}$ (Price et al. 2014). As this relation was derived by assuming the Calzetti et al. (2000) attenuation curve for both the continuum and line emission, we convert the inferred nebular attenuation to the Cardelli et al. (1989) curve, and correct the Hα fluxes accordingly. In order for Hβ to be used in the dust correction, it must be detected with a signal-to-noise ratio (S/N) ≥ 3, and the spectrum transmission at Hβ must be at least 50% of the maximum transmission.

The dust-corrected Hα fluxes are converted into Hα luminosities, that are then used to calculate the Hα SFRs following the relation of Kennicutt (1998) for a Chabrier (2003) IMF (Shivaei et al. 2015). Finally, the relation between $\Sigma_{\rm gas}$ and $\Sigma_{\rm SFR}$ by Kennicutt (1998) is used to estimate the gas masses, using $\Sigma_{\rm gas} = M_{\rm gas}/(\pi R_E^2)$ and $\Sigma_{\rm SFR} = {\rm SFR}/(\pi R_E^2)$, where R_E is the best-fit GALFIT major axis. In Section 5.7 we discuss the validity of this relation at high redshift. The gas mass uncertainties include uncertainties on the Hα and Hβ fluxes and on the slit-loss corrections. An uncertainty of 0.2 dex on $A_{\rm V,cont,Calzetti}$ is assumed when Hβ is undetected.

2.2. *Sample selection*

For this work, we select objects in the redshift ranges $1.34 \leq z \leq 1.75$ and $2.075 \leq z \leq 2.6$, to ensure coverage of the Hα emission line. We also require that Hα is detected (i.e., S/N $\geq$ 3), and that there is *HST*/F160W coverage, to make use of the GALFIT structural parameter measurements.

We use additional selection criteria to ensure we include only high-quality spectra. First, we consider only primary MOSDEF targets, excluding any serendipitously detected galaxies that happened to fall within the slit. Second, we exclude objects with non-negligible contamination to the Hα flux from neighboring skylines, to provide clean kinematic measurements. Third, we impose quality cuts for both the stellar population and structural parameters to ensure that the best fits adequately model the data. For the stellar population fits, we exclude objects for which the best-fit reduced chi-square $\chi^2_{\rm red} > 10$. For the structural parameters, we flag and exclude objects for which *(a)* the GALFIT runs did not converge, or *(b)* the GALFIT and *HST*/F160W total magnitudes differ by more than 0.5 mag. Fourth, we exclude any objects that fall within the quiescent region in the UVJ diagram (Wuyts et al. 2007, Williams et al. 2009). Fifth, we exclude AGN with outflow signatures or with very broad emission lines (Freeman et al. in preparation). Sixth, we exclude objects that appear to have an interacting counterpart at a similar redshift, as the velocity signatures of these systems may not reflect the internal kinematics. We consider AGN, as identified by their X-ray luminosity, IRAC color, or rest-frame optical emission lines ratios (Coil et al. 2015, M. Azadi et al. in preparation) separately from our sample of star-forming galaxies.

Our final sample includes 178 unique galaxies, with Hβ detected in 138. One object has been observed twice. We also consider 21 unique AGN (14 with Hβ detected) that meet all selection criteria, with 2 AGN having been observed twice.

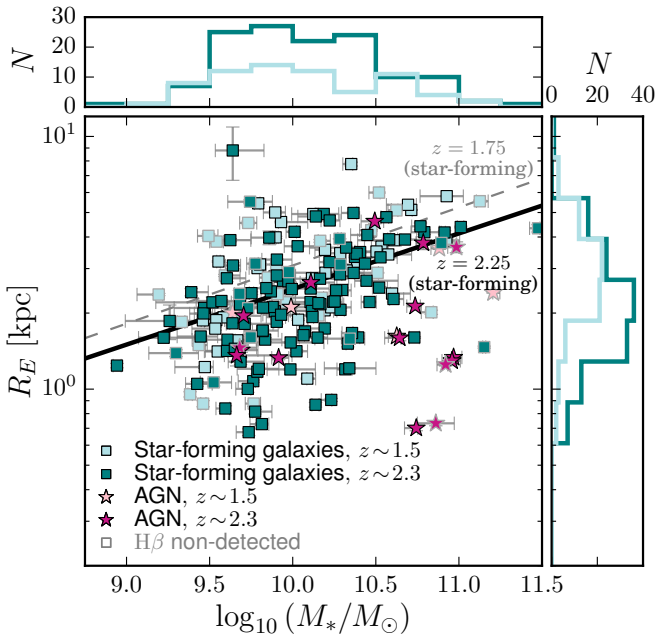

FIG. 1.— Effective radius, R_E, versus stellar mass, $\log_{10}(M_*/M_\odot)$, for the galaxies and AGN in our sample, split by redshift range. The galaxies at in the lower ($z \sim 1.5$) and higher ($z \sim 2.3$) redshift ranges are shown as light blue and teal squares, respectively. The AGN in the same redshift ranges are shown as pink and purple stars, respectively. Histograms of R_E and $\log_{10}(M_*/M_\odot)$ show the objects (galaxies and AGN) in the lower (light blue) and higher (teal) redshift ranges. Galaxies (and AGN) without Hβ detections are marked with grey outlines. The black solid and grey dashed lines represent the best-fit size-stellar mass relations for star-forming galaxies from van der Wel et al. (2014a) at $z = 2.25$ and $z = 1.75$, respectively. Our sample of star-forming galaxies generally follow the best-fit size-stellar mass relations.

We show the effective radii versus stellar masses for the galaxies and AGN in our sample in Figure 1. For comparison, we also show the best-fit size-stellar mass relations found by van der Wel et al. (2014a) for a complete sample of star-forming (late-type) galaxies at $z = 2.25$ and 1.75. The samples are complete down to $M_* \sim 10^{9.5} M_\odot$ at $z = 2.25$ and down to $M_* \sim 10^{9.1} M_\odot$ at $z = 1.75$, and are therefore a good representation of the star-forming galaxies at these redshifts. Our galaxies generally follow these best-fit size-stellar mass relations in both redshift ranges, though our galaxies at $z \sim 1.5$ may be somewhat smaller in size than the average as determined by van der Wel et al. (2014a).

3. KINEMATIC MEASUREMENTS

We measure the kinematic properties of our galaxy sample from the Hα emission lines in combination with the *HST*/F160W structural parameters. For objects with spatially-resolved rotation curves, we constrain the rotation and dispersion velocity components by fitting models to the 2D Hα emission lines, as discussed in Section 3.1. The kinematics for objects without detected rotation are constrained from the 1D Hα profile, by simultaneously fitting Hα and [NII] lines following the method listed in Section 3.2. In Section 3.3, we determine for which objects we may reasonably expect to see rotation and for which we do not expect to see rotation at all. We compare these expectations with our observations and discuss what this may tell us about the kinematic structures of galaxies. The method for calculating the dynamical masses is

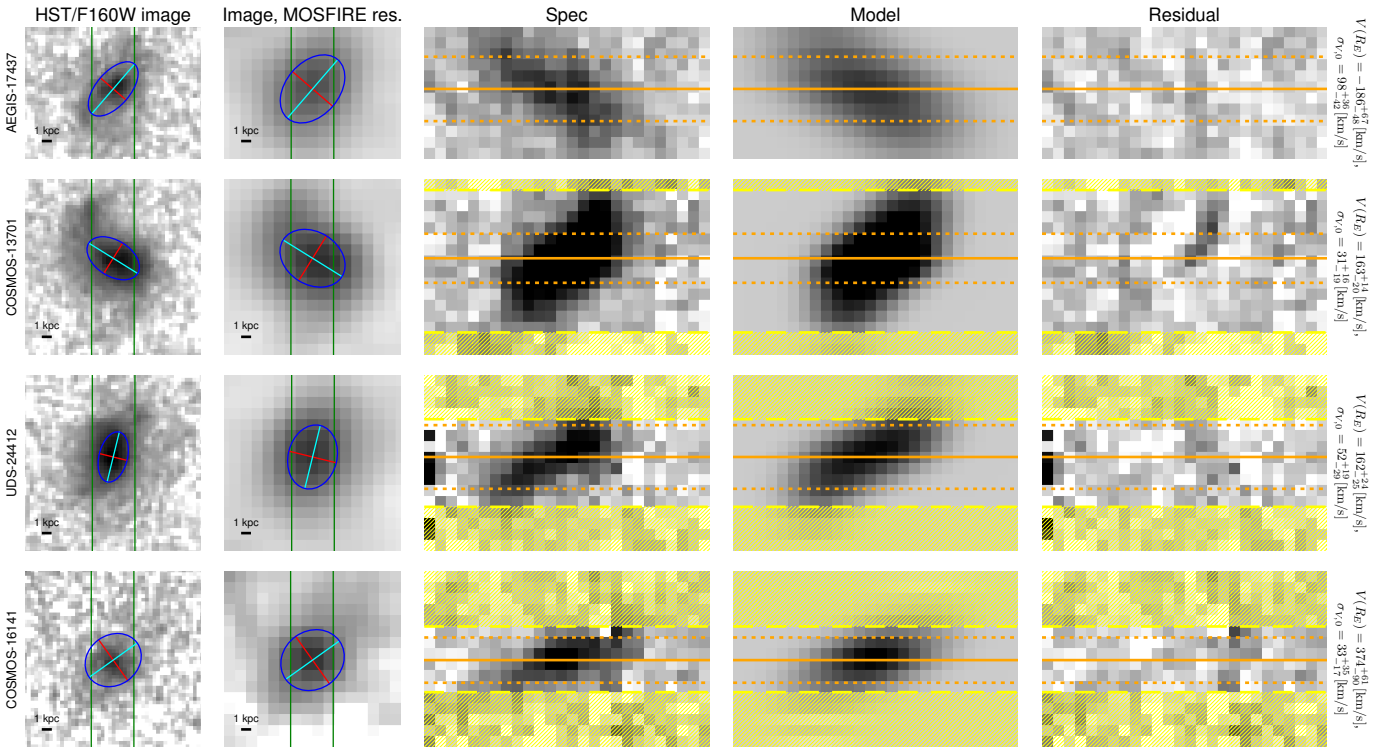

FIG. 2.— Example overviews of the spatially resolved kinematic modeling, as described in Section 3.1. The first column shows the *HST*/F160W image, the slit position (green lines) and the GALFIT half-light ellipse (major axis in cyan, minor axis in red, ellipse in blue). The second column shows the *HST*/F160W image convolved to match the seeing resolution of the MOSFIRE spectra, with the GALFIT parameters similarly convolved. The third column shows the continuum-subtracted 2D spectrum centered at Hα. The fourth column shows the best-fit kinematic model to the line emission. The fifth column shows the residual between the 2D spectrum and the best-fit model, on the same grey scale as the 2D spectrum. In the third-to-fifth columns, the vertical and horizontal axes are the spatial position and wavelength, respectively. The orange horizontal line shows the best-fit model center, y_0, with the dotted lines showing the convolved and projected R_E, and the yellow shading and yellow dashed lines indicate low signal-to-noise rows that are masked in the fitting procedure. For each object, the field and 3D-HST v4 ID number are shown at the left, and the best-fit $V(R_E)$ and $\sigma_{V,0}$ are given on the right.

discussed in Section 3.4. Finally, in Section 3.5, the 2D and 1D kinematic measurement methods are compared using the galaxies with rotation.

3.1. *Rotation velocity measurements*

In this section we constrain the rotational velocity and velocity dispersion simultaneously by modeling the 2D spectra in combination with the F160W structural parameters for each MOSDEF galaxy in our sample. Previous studies have presented methods for fitting 2D spectra, including Vogt et al. (1996), Simard & Pritchet (1999), and Weiner et al. (2006). However, the models of Simard & Pritchet (1999) and Weiner et al. (2006) do not account for misalignment between the slit and major axis, while Vogt et al. (1996) and Simard & Pritchet (1999) exclude velocity dispersion.

Instead, we define kinematic models that explicitly include the position angle misalignment and inclination, and simultaneously fit the rotation velocity and velocity dispersion. The kinematic models are discussed in detail in Appendix A.1. In summary, the kinematic models include both rotation and a constant velocity dispersion over the galaxy, and have a total of 3 free parameters: the asymptotic velocity (V_a) and turnover radius (r_t) of the arctan rotation curve model, and the constant intrinsic velocity dispersion ($\sigma_{V,0}$). We assume the best-fit GALFIT parameters and the position angles from the F160W observations. The model is collapsed along the line-of-sight, and convolved to match the seeing conditions of each spectrum. Using the position angle, inclination, brightness profile, and seeing information, we determine what portions of the model fall within the slit for each object. Finally, the model is collapsed in the spatial direction perpendicular to the slit and convolved by the instrumental resolution.

To fit the emission lines, we start by subtracting the continuum from each Hα 2D spectrum. We also trim the spectrum to exclude the [NII] emission lines and to include only the positive emission line image. We then construct a mask for the emission line spectrum to exclude missing data and low signal-to-noise rows from our fitting procedure. A detailed description of this procedure can be found in Appendix A.2.

We then find the best-fit models to the trimmed 2D Hα spectra and the corresponding confidence intervals by performing parameter space exploration using the `python` Markov-Chain Monte Carlo (MCMC) package `emcee` (Foreman-Mackey et al. 2013), following the method detailed in Appendix A.2. As the rotation curve turnover is not well constrained in our data, there is a degeneracy in the values of V_a and r_t. Nonetheless, the values of $V(R_E)$ and $V_{2.2} = V(2.2r_s)$ (assuming the arctan rotation curve model, see Equation A6) are well constrained. We note that we explicitly include the structural parameters and projection effects in our model, so we directly constrain the intrinsic galaxy parameters, without projection or blending effects. Examples of the 2D Hα emission line fits are shown in Figure 2.

We use the values of $V(R_E)$ to determine which objects have spatially resolved rotation. We take objects with $V(R_E) \neq 0$ within the 95% one-sided distribution to be our sample with resolved rotation, and the objects that fail this cut

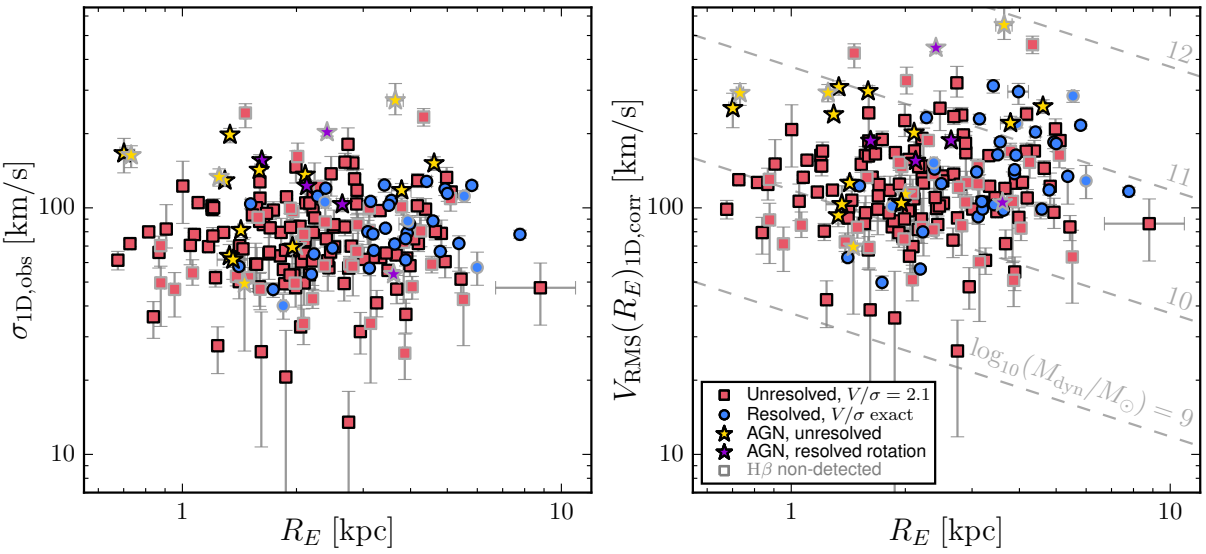

FIG. 3.— Observed velocity dispersion $\sigma_{1D,obs}$ (left) and the corrected velocities $V_{RMS}(R_E)_{1D,corr}$ (right) vs. R_E. The corrections for the galaxies without resolved rotation (red squares) are derived assuming $\left[(V/\sigma_{V,0})_{R_E}\right]_{2D,median} = 2.1$. For comparison, the corrections for the galaxies with resolved rotation, derived using the measured $(V/\sigma_{V,0})_{R_E}$ of each object, are shown as well (blue circles). We also show the AGN in our sample, and denote those with and without resolved rotation by purple and yellow stars, respectively. Galaxies (and AGN) without Hβ detections are marked with grey outlines. Lines of constant dynamical mass, calculated using Equation 3 and assuming $(V/\sigma_{V,0})_{R_E} = 2.1$, are shown in the right panel (dashed grey lines). The RMS velocities are on average a factor of ~ 2 larger than the observed values.

to be our dispersion-only sample. The position-velocity diagrams of the 35 galaxies with detected rotation are shown in Appendix A.3.

3.2. *Integrated velocity dispersion measurements*

For all objects without resolved rotation (see Section 3.1), we measure the kinematics from the 1D spectra. As our sample consists of star-forming galaxies, we may expect that their intrinsic velocity support is at least partially rotational. This assumption is reinforced by the work of Newman et al. (2013), who find that galaxies that were initially classified as dispersion-dominated in fact do show evidence for rotation in observations with higher spatial resolution. Thus, we model the composite unresolved kinematics by assuming a value for $(V/\sigma_{V,0})_{R_E} = V(R_E)/\sigma_{V,0}$, while taking into account the GALFIT parameters and seeing conditions. We then use this model to convert the measured velocity dispersion to intrinsic quantities.

We measure the velocity dispersion from the optimally extracted 1D spectra by fitting Hα, the [NII] doublet, and the continuum simultaneously with a triple Gaussian and a linear component. We fit the spectrum between $6480\text{Å} \leq \lambda/(1+z_{MOS}) \leq 6650\text{Å}$, and mask pixels with no coverage. We vary the coupled line centers, while constraining $\lambda_{H\alpha,obs}$ to within ± 20Å of $\lambda_{H\alpha}(1+z_{MOS})$. The widths of the emission lines (in Å) are coupled in velocity space, with $\sigma_{\lambda,[NII]\lambda\lambda6584,48} = \sigma_{\lambda,H\alpha}\,(\lambda_{[NII]\lambda\lambda6584,48}/\lambda_{H\alpha})$. We also assume $F([NII]\lambda6548) = 1/3\,F([NII]\lambda6584)$ (Osterbrock & Ferland 2006). Finally, we enforce $\sigma_{\lambda,H\alpha} \geq \sigma_{\lambda,sky}$, with the instrumental resolution measured from the median skyline width.

The Hα line widths are corrected for the line broadening due to the instrumental resolution by subtracting $\sigma_{\lambda,sky}$ in quadrature from $\sigma_{\lambda,H\alpha}$. Each corrected Hα line width $\sigma_{\lambda,H\alpha,corr}$ is converted to an observed velocity dispersion, $\sigma_{V,obs}$, using the best-fit redshift.

The errors on the observed velocity dispersions are estimated by creating 500 realizations where the spectra are perturbed according to the corresponding error spectra. We then perform the same fitting and correction procedure on the perturbed spectra, and convert the corrected line widths to velocity dispersions using the best-fit redshift of each realization.

For each object, we convert the observed velocity dispersion into an intrinsic root mean square (RMS) velocity, $V_{RMS} = \sqrt{V^2 + \sigma_V^2}$, which explicitly includes both intrinsic rotation and dispersion velocities. This method is discussed in detail in Appendix B. In summary, we model each object as an inclined disk (using the GALFIT structural parameters R_E, n, b/a), with the major axis offset from the slit by ΔPA. The rotation and velocity dispersion kinematics are included by assuming a fixed ratio of $(V/\sigma_{V,0})_{R_E}$, and then the model is convolved to match the MOSFIRE seeing resolution. We determine which portions of the model fall within the slit width and the extracted width in the spatial direction, and then apply the optimal-extraction weighting. For this model, we calculate the ratio of the luminosity-weighted second velocity moment ($\sigma_{V,model}$) to the RMS velocity at R_E ($V_{RMS}(R_E)_{model}$), and use this ratio to convert the observed, integrated velocity dispersion to the composite RMS velocity at R_E following

$$V_{RMS}(R_E)_{1D,corr} = \sigma_{V,obs}\left(\frac{\sigma_{V,model}}{V_{RMS}(R_E)_{model}}\right)^{-1}. \quad (2)$$

van Dokkum et al. (2015) use an α parameterization to infer a rotational velocity from an observed velocity dispersion. This α value is empirically derived and combined with an inclination correction, with $\alpha = \sigma_{V,obs}/(V \sin i)$. Hence, this correction does not take into account the exact portion of the galaxy observed through the slit or partial support from random motions. However, the galaxies by van Dokkum et al. are in general smaller than those in our sample, and will suffer less from slit losses.

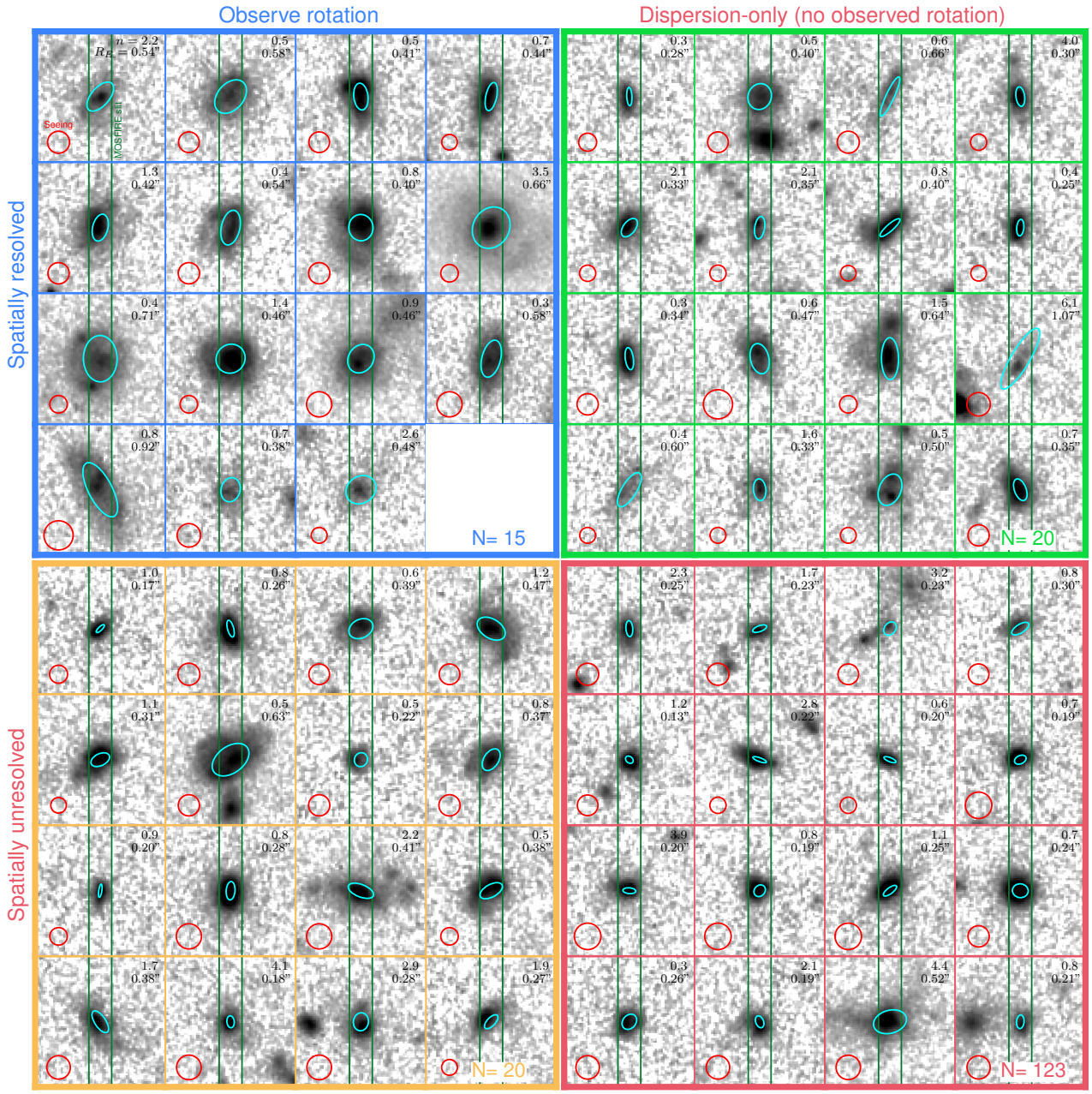

FIG. 4.— *HST*/F160W galaxy images ($4'' \times 4''$) for each of the 4 spatial/kinematic resolution categories: spatially resolved with observed rotation (upper left panel, blue), spatially unresolved with observed rotation (lower left, yellow), spatially resolved with only dispersion observed (upper right, green), and spatially unresolved with only dispersion observed (lower right, red). Each image is centered on the object center. The slit positions and orientations are shown with the green lines. We represent the GALFIT effective radius (R_E, measured from the major axis), axis ratio (b/a), and position angle relative to the slit (ΔPA) for each object with the cyan ellipses. The values of R_E and the Sérsic index n are annotated in the upper-right corners of the images. The atmospheric seeing FWHMs are shown with the red circles. The total number of objects in each of the 4 categories is displayed in the lower right corner of each quadrant. Spatially close companions of the target objects are located at different redshifts.

In Figure 3 we show $\sigma_{V,\,\rm obs}$ and $V_{\rm RMS}(R_E)_{\rm corr}$ vs. R_E for galaxies and AGN without detected rotation. For now, we assume $(V/\sigma_{V,0})_{R_E} = 2.1$, the median of the values measured for galaxies with detected rotation. For reference, we also show the velocity dispersions measured from the integrated 1D spectra of the galaxies with detected rotation, with the corrections for these objects calculated using the exact $(V/\sigma_{V,0})_{R_E}$ measured for each object. The median observed 1D velocity dispersion for our sample with $M \geq 10^{9.5} M_\odot$ (the approximate completeness limit for star-forming galaxies in the MOSDEF survey, see Shivaei et al. 2015) is $(\sigma_{V,\,\rm obs})_{\rm median} = 78$ km/s. The median observed velocity dispersion $(\sigma_{V,\,\rm obs})_{\rm median} = 70$ km/s of the galaxies at $z \sim 1.5$ is slightly lower than the value of $(\sigma_{V,\,\rm obs})_{\rm median} = 80$ km/s for the galaxies at $z \sim 2.3$.

3.3. *Resolved vs. unresolved kinematics*

As our primary sample consists of star-forming galaxies, in Section 3.2 we have treated the objects for which we only observe velocity dispersion as being intrinsically disks, with some amount of thickening. Here we consider whether this is a reasonable assumption by considering the necessary condi-

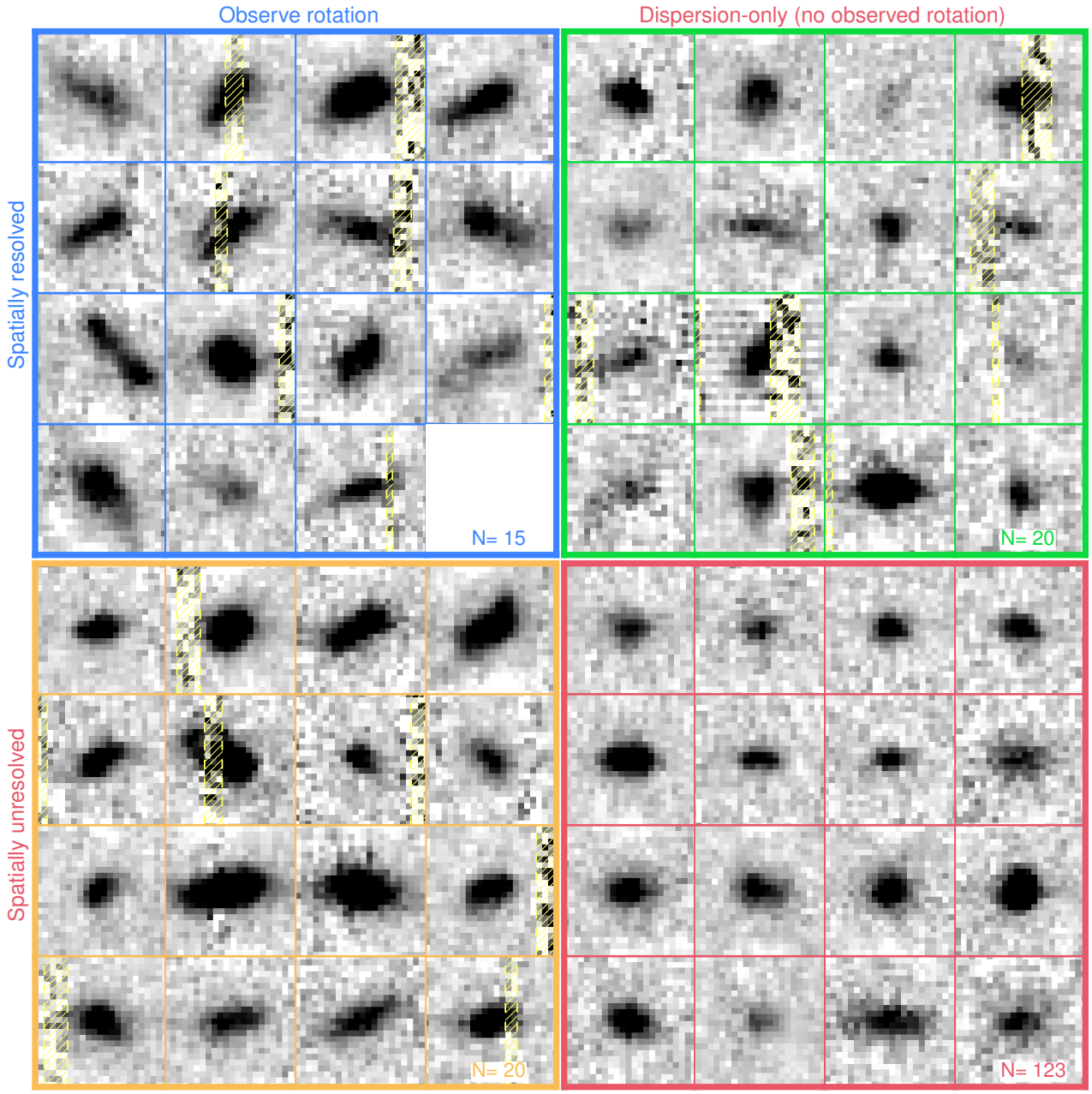

FIG. 5.— MOSFIRE spectra centered on Hα for galaxies in the 4 spatial/kinematic resolution categories. The displayed galaxies are the same as those shown in Figure 4, with each object vertically centered on the same position and same spatial scale as the *HST*/F160W images. The horizontal axis shows wavelength, where each stamp spans ~ 36 Å (H band) or ~ 48 Å (K band) in the observed frame.

tions to observe rotation in a galaxy.

One reason why intrinsic rotation may not be observable is that the galaxy is small with respect to the seeing size. If there is only one resolution element across the galaxy disk, then any rotation signature will be washed out and we would only observe velocity dispersion. Additionally, the galaxy major axes may be misaligned with the slit axis. A position angle (PA) offset reduces the ability to detect rotation, as for more misaligned objects, the rotational information is projected into fewer resolution elements along the slit. At the most extreme, if a galaxy is completely misaligned with the slit (i.e. $\Delta\mathrm{PA} = 90°$), the rotational signature is collapsed into the same resolution element, and again we would only observe a velocity dispersion.

We consider the dual effects of object size and ΔPA, by calculating how much of the stellar light major axis falls within the slit, projected along the slit direction. The projected size of the object falling within the slit ($2\,R_{E,\mathrm{proj}}$) should be larger than the seeing for the object to be spatially resolved, or $R_{E,\mathrm{proj}} \geq \mathrm{FWHM}_{\mathrm{seeing}}/2$.

We divide our sample into four categories, based on combination of the projected spatial resolution criterion given above (resolved vs. unresolved) and whether we detect rotation or not (rotation vs. dispersion, see Section 3.1). This classification scheme gives 15 spatially resolved galaxies with observed rotation, 20 spatially unresolved galaxies with observed rotation, 20 spatially resolved galaxies with only dispersion observed, and 123 spatially unresolved galaxies with

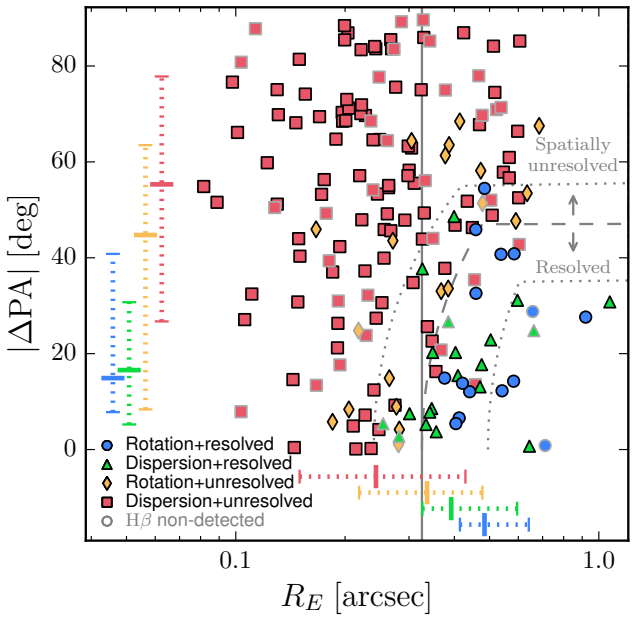

FIG. 6.— The position angle (PA) offset between the slit and photometric major axis versus the effective radius (R_E) for galaxies in our sample. The color coding is based on whether we observe rotation or not (rotation vs. dispersion), and whether the projected major-axis is larger than the seeing size or not (spatially resolved vs. unresolved). The colored lines denote the median R_E and $|\Delta\mathrm{PA}|$ for each subsample, with the dotted lines showing the 68% value ranges. Galaxies without Hβ detections are marked with grey outlines. The vertical grey line denotes 1/2 the median seeing FWHM ($0\farcs65$) for our sample. The dashed grey line shows the division between spatially resolved and unresolved objects described in Section 3.3, assuming the median seeing. Objects to the right and below this line would be classified as spatially "resolved" (assuming they were observed under the median seeing conditions), while objects to the left and above would be classified as spatially "unresolved". The upper and lower dotted grey lines show the dividing lines if the seeing were equal to the minimum ($0\farcs48$) and maximum ($0\farcs99$) effective seeing conditions, respectively (see Table 1, Kriek et al. 2015).

only dispersion observed. In Figures 4 & 5 we show example *HST* images and spectra, respectively, for objects in each category.

We show PA offset versus object size (R_E) as a function of seeing in Figure 6. At fixed R_E, we tend to have more "dispersion-only" objects and fewer objects with detected rotation as the position angle offset increases from aligned (0°) to completely misaligned (90°). We also note that on average, galaxies for which we observe rotation tend to be larger than those without observed rotation. This finding supports the possibility that we may not observe rotation for some objects simply because they are physically too small to resolve, even if there is no position angle offset between the semi-major axis and the slit. We can also see these trends in Figure 4, as the objects with observed rotation (left panels) tend to have better alignment between their major axes and the slit, and tend to have larger angular sizes relative to the objects for which we only observe dispersion (right panels).

However, not all objects follow the expected classifications. For instance, we observe rotation for some spatially unresolved objects. These galaxies are shown as yellow diamonds in Figure 6, with example images and spectra shown in the lower left panels of Figures 4 and 5. Also, if all galaxies in our sample are intrinsically disk galaxies and have at least partial rotational support, we would expect to see rotation in all objects that are spatially resolved. Yet we do not observe rotation in some of the galaxies that meet the projected spatial resolution criterion, which are shown as green triangles in Figure 6, with examples in the upper right panels of Figures 4 and 5.

Other effects may influence the classification of our sample into these four sub-samples, which could explain why we see objects in the unexpected classification categories. First, the position angle offset between the kinematic major axis and the slit could be incorrect. This error may be due to uncertainties in the photometric major axis position angle estimation or to a misalignment between the kinematic and photometric major axes. The latter effect has been observed by Wisnioski et al. (2015) in galaxies at $z \sim 2$, and possibly indicates disturbed kinematics due to mergers (Epinat et al. 2012). If the position angle offset is incorrect, our projected size along the major axis may not match the true intrinsic projected size of the region that we probe with the kinematics. Thus objects may scatter from the "spatially resolved" category into the "spatially unresolved" category or vice versa.

Second, we use the rest-frame optical R_E in this classification, but we measure the kinematics from Hα emission. We show in Section 5.6 that the rest-frame optical and Hα sizes of the galaxies with detected rotation are very similar, so using R_E to determine spatial resolution is a reasonable approximation. Still, if an object is close to the detection limit, small differences between R_E and Hα size could change the spatial resolution classification.

Third, we do not incorporate inclination angle in our classification procedure. For face-on galaxies, we do not expect to detect rotation. If we consider galaxies with $b/a \geq 0.9$ (i.e., $i \lesssim 26°$, assuming $(b/a)_0 = 0.19$) to be face-on, only 5 of our galaxies satisfy this criterion, three of which have detected rotation, and two of which had been classified as "spatially resolved".

Fourth, we rely on single-component GALFIT fits to determine the photometric position angle, axis ratio b/a, and stellar effective radius R_E. Our galaxies often exhibit clumps, so they are not perfectly fit by a smooth Sérsic profile. Furthermore, GALFIT is unable to recover extreme inclination angles (i.e., close to edge-on or face-on; Epinat et al. 2012). These limitations could further influence the accuracy of the position angle, effective radius, and axis ratio, and could influence whether an individual galaxy is categorized as "spatially resolved" or not.

Fifth, the S/N of the observed spectra will influence the object kinematic categorization. Our 95% one-sided $V(R_E)$ detection requirement may result in classifying objects with intrinsic rotation but low S/N spectra as "dispersion-only." The example spectra in Figure 5 in the spatially-resolved, dispersion-only quadrant (green upper-right panel) do appear to have either similar or lower signal-to-noise ratios relative to the spectra of the objects with detected rotation (shown in the left panels).

Sixth, neighboring skylines may overlap portions of a rotation curve, which may also cause an object to fail the $V(R_E)$ detection criterion. In Figure 5, we see some objects in the green quadrant with signifiant overlap with skyline contaminated columns (i.e., the fourth object, top row, and second object, third row, of the green, upper-right quadrant of Figure 5).

Between the four categories, 89% of the objects are consistent with having rotation. This includes the 69% of the galaxies that are unresolved and have no detected rotation, for which the kinematic structures of the individual galaxies are

unknown. In Section 4.2, we find that galaxies without detected rotation are consistent with having kinematic support from both rotation and random motions. The only galaxies inconsistent with the assumption of intrinsic rotational support are those that are spatially resolved without observed rotation (green objects, Figure 6). However, as mentioned previously, there are sources of uncertainty in our categorizations that may imply these objects may still have intrinsic rotation.

3.4. *Dynamical mass measurements*

We combine the kinematic and structural information to calculate the dynamical masses of our galaxies. The rotation and dispersion velocities are combined by taking the RMS velocity, $V_{\rm RMS}(R_E) = \sqrt{\sigma_{V,0}^2 + V(R_E)^2}$, and we calculate the total dynamical mass as

$$M_{\rm dyn} = k_{\rm eff} \frac{V_{\rm RMS}(R_E)^2 R_E}{G}, \quad (3)$$

where G is the gravitational constant. Here we define an "effective" virial coefficient to account for the relative contribution to the RMS velocity from the rotation and dispersion velocities (i.e., including an "asymmetric drift" correction from the velocity dispersion, as in Meurer et al. 1996, Epinat et al. 2009, Daddi et al. 2010, Newman et al. 2013):

$$k_{\rm eff} = \frac{k_{\rm disp} + k_{\rm rot}((V/\sigma_{V,0})_{R_E})^2}{1 + ((V/\sigma_{V,0})_{R_E})^2}, \quad (4)$$

where $(V/\sigma_{V,0})_{R_E} = V(R_E)/\sigma_{V,0}$.[1] We assume $k_{\rm disp} = 5$ as the virial coefficient corresponding to the dispersion kinematic component, from the simple case of a sphere of uniform density (Pettini et al. 2001). We estimate the virial coefficient for the rotational kinematic component following Miller et al. (2011), who find $k = 1.33$ for the dynamical mass within $r = 2.2r_s = 1.3R_E$. To convert to the total dynamical mass, we approximate $k_{\rm rot} \approx 2k = 2.66$.

To calculate $k_{\rm eff}$ and the dynamical masses, we use the best-fit values of $V(R_E)$ and $\sigma_{V,0}$ measured in Section 3.1 for the galaxies with detected rotation. For the galaxies without observed rotation, we have to assume a value of $(V/\sigma_{V,0})_{R_E}$ to calculate $k_{\rm eff}$, $V_{\rm RMS}(R_E) = V_{\rm RMS}(R_E)_{\rm 1D,\,corr}$, and $M_{\rm dyn}$. We will discuss the assumption of $(V/\sigma_{V,0})_{R_E}$ in Section 4.

3.5. *Dynamical mass method comparison: spatially resolved galaxies*

We test the method for correcting the kinematics of disk galaxies without detected rotation using the spatially-resolved rotation sample of galaxies, for which we have more detailed kinematic information.

First, we measure the dynamical masses $M_{\rm dyn,\,2D}$ using the exact values of $V(R_E)$ and $\sigma_{V,0}$ from the 2D spectral fitting method in Section 3.1. We then measure the velocity dispersions from the optimally-extracted 1D spectra for the same sample of galaxies. We assume the exact $(V/\sigma_{V,0})_{R_E} = V(R_E)/\sigma_{V,0}$ measured from the 2D spectral fitting for each object to calculate the corrected 1D velocity dispersions (Equation 2), $k_{\rm eff}$ (Equation 4), and the resulting dynamical masses $M_{\rm dyn,\,1D}$.

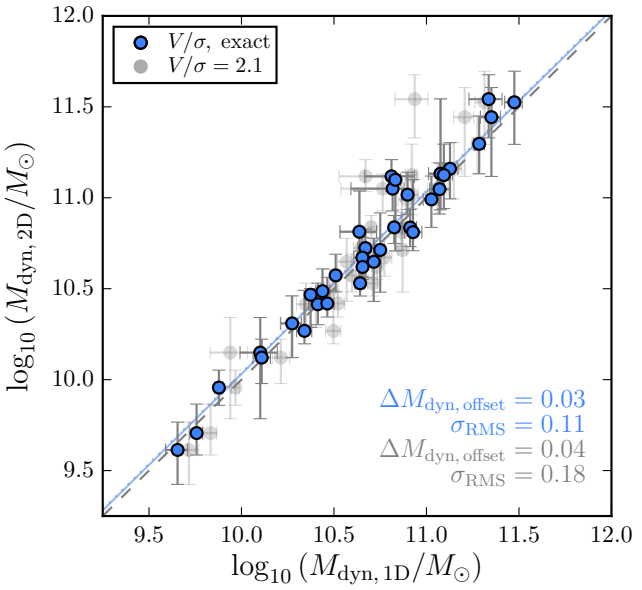

FIG. 7.— Comparison of the dynamical mass measurement methods. The masses of the galaxies with observed rotation are measured with both the resolved kinematic information ($M_{\rm dyn,\,2D}$) and from the aperture-corrected optimally-extracted 1D-spectra ($M_{\rm dyn,\,1D}$) assuming the exact value of $(V/\sigma_{V,0})_{R_E}$ for each objects (blue circles). There is little scatter ($\sigma_{\rm RMS} = 0.11$ dex) between the two measurements, and a small median offset $\Delta M_{\rm dyn} = 0.03$ dex (blue line), with $M_{\rm dyn,\,2D}$ being slightly higher than $M_{\rm dyn,\,1D}$. If instead a constant $(V/\sigma_{V,0})_{R_E} = 2.1$ were assumed in calculating the 1D velocity dispersion corrections (grey circles) the median offset (dotted grey line) and scatter are slightly larger ($\Delta M_{\rm dyn} = 0.04$ dex, $\sigma_{\rm RMS} = 0.18$ dex). Nonetheless, there is still excellent agreement between the measurements.

We compare $M_{\rm dyn,\,1D}$ with $M_{\rm dyn,\,2D}$ in Figure 7. The corrected $M_{\rm dyn,\,1D}$ values are in excellent agreement with the $M_{\rm dyn,\,2D}$ values, with little scatter between them ($\sigma_{\rm RMS} = 0.11$ dex). We find a median offset of $\Delta \log_{10} M_{\rm dyn,offset} = 0.03$ dex between the two measurements, such that the 2D-kinematic derived values of $M_{\rm dyn}$ are slightly larger than the values derived from the aperture-corrected 1D spectra.

However, if these galaxies would not have been resolved, we would not have known their intrinsic $(V/\sigma_{V,0})_{R_E}$, to be used in the dynamical mass estimate. Thus, we also calculate $M_{\rm dyn,\,1D}$ using the median $[(V/\sigma_{V,0})_{R_E}]_{\rm 2D,median} = 2.1$ for each object (shown as the grey points in Figure 7). We find a slightly larger offset ($\Delta \log_{10} M_{\rm dyn,offset} = 0.04$ dex) and scatter ($\sigma_{\rm RMS} = 0.18$ dex). Hence, for the galaxies with detected rotation, assuming the average value of $(V/\sigma_{V,0})_{R_E}$ for each object yields dynamical masses that are nearly as accurate as the dynamical masses derived from the rotation curves. Based on this test, we conclude that the 1D velocity dispersion correction method works well, and should produce reasonable dynamical masses for the remainder of the galaxies without observed rotation if the average $(V/\sigma_{V,0})_{R_E}$ is known.

4. RESULTS

We now consider the total sample, combining the samples with and without observed rotation, and compare the dynamical and the baryonic masses, and assess the kinematic structures of star-forming galaxies at $z \sim 2$.

[1] Note that when $(V/\sigma_{V,0})_{R_E} \to \infty$ (i.e. only rotational support), we have $V_{\rm RMS}(R_E) = V(R_E)$ and $k_{\rm eff} \to k_{\rm rot}$, and Equation 3 is equivalent to the dynamical mass assuming only rotational support, $M_{\rm dyn} = k_{\rm rot} V(R_E)^2 R_E/G$. In the opposite limit, when $(V/\sigma_{V,0})_{R_E} = 0$ (i.e. only pressure support), we have $V_{\rm RMS}(R_E) = \sigma_{V,0}$ and $k_{\rm eff} = k_{\rm disp}$, and we recover the case for pressure-only support: $M_{\rm dyn} = k_{\rm disp}\sigma_{V,0}^2 R_E/G$.

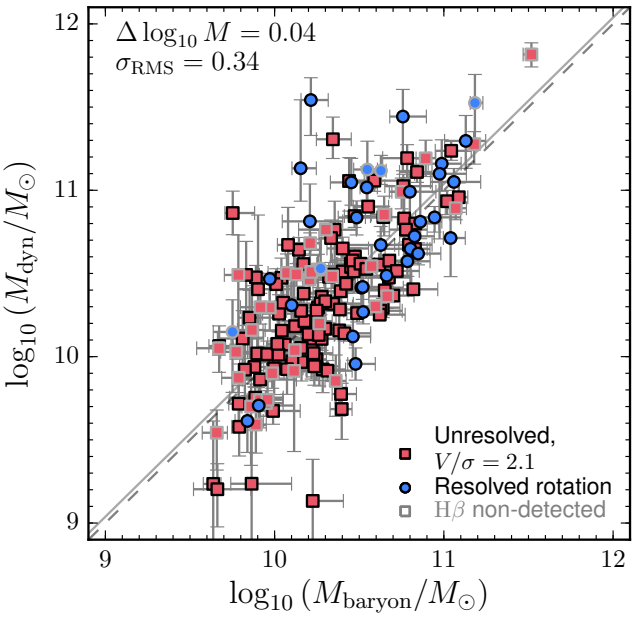

FIG. 8.— Comparison of dynamical and baryonic (stellar + gas) masses for all galaxies in our sample. Symbols are similar as in Figure 3. To calculate the velocity corrections for the sample without observed rotation, we assume the median $(V/\sigma_{V,0})_{R_E} = 2.1$ from the sample with observed rotation. The grey dashed line indicates equal $M_{\rm baryon}$ and $M_{\rm dyn}$, and the solid grey line indicates the median offset of $\Delta \log_{10} M = \log_{10} M_{\rm dyn} - \log_{10} M_{\rm baryon}$. The scatter of the data around the median offset is $\sigma_{\rm RMS} = 0.34$ dex. The error bars do not include the systematic uncertainties discussed in Section 5.7.

4.1. *Comparison of dynamical and baryonic masses*

In order to measure the dynamical masses for all galaxies in our sample, we need a $(V/\sigma_{V,0})_{R_E}$ ratio for the galaxies without resolved kinematics. We assume that the kinematically resolved objects have a similar structure as the unresolved objects, and adopt the median $(V/\sigma_{V,0})_{R_E} = 2.1$ as measured from the rotation objects (see Section 3.1 and Appendix A).

In Figure 8 we compare the dynamical masses to the baryonic masses, $M_{\rm baryon} = M_* + M_{\rm gas}$ (as given in Section 2.1). They show a remarkable agreement, with a median offset of $\Delta \log_{10} M = 0.04$ dex, where $M_{\rm dyn}$ is slightly larger than $M_{\rm baryon}$ at a given $M_{\rm baryon}$. The scatter about the median $\Delta \log_{10} M$ is low, with $\sigma_{\rm RMS} = 0.34$ dex. Additionally, objects with and without detected rotation follow the same $M_{\rm baryon} - M_{\rm dyn}$ relation, which may support the assumption that the galaxies are all intrinsically rotating disks. We will investigate this in more detail in the next section.

The offset between the masses implies a dark matter fraction within R_E of 8%. This fraction is lower than the $\sim 30-50\%$ dark matter fractions within 2.2 r_s for disk galaxies at $z \sim 0$ (which increase with decreasing stellar mass; Pizagno et al. 2005, Dutton et al. 2011a), and the $\sim 20-30\%$ within $r < 10$ kpc at $z \sim 2$ (Förster Schreiber et al. 2009). This is expected, as these studies consider larger radii, and the dark matter fraction increases with increasing radius. Additionally, our measurement is dependent on several systematic uncertainties that we discuss in Section 5.7.

4.2. *Rotational versus pressure support for unresolved galaxies*

In the previous section we simply assumed that all kinematically resolved and unresolved objects have a similar median $(V/\sigma_{V,0})_{R_E}$. However, from Figure 6 we know that on average the unresolved objects are smaller, and thus they may be structurally different. In this section we use the average properties of the sample without resolved rotation to independently estimate the average $(V/\sigma_{V,0})_{R_E}$ for these objects.

The effects of varying the $(V/\sigma_{V,0})_{R_E}$ for all objects without observed rotation are demonstrated in Figure 9. In the left panel, we show the assumption of $(V/\sigma_{V,0})_{R_E} \rightarrow \infty$, or no intrinsic velocity dispersion, for the objects without detected rotation. For comparison, we show the galaxies with detected rotation, using the the dynamical masses calculated from the rotation velocities and velocity dispersions measured from the 2D fitting procedure (see Section 3.1). There is a positive correlation between the mass offset $\Delta \log_{10} M$ and b/a with Spearman correlation coefficient $\rho = 0.18$ at 2.2σ. We quantify this trend by fitting a line to median binned $\Delta \log_{10} M$ and b/a in bins of b/a. This trend of increasing $M_{\rm dyn}$ relative to $M_{\rm baryon}$ as b/a increases indicates that we have over corrected for inclination, and that our assumption of $(V/\sigma_{V,0})_{R_E} \rightarrow \infty$ is too extreme.

If we instead assume lower values of $(V/\sigma_{V,0})_{R_E}$, the inclination correction will be reduced at higher b/a, resulting in a reduced mass offset. Hence, we can constrain $(V/\sigma_{V,0})_{R_E}$ for the galaxies without detected rotation by examining the offset $\Delta \log_{10} M = \log_{10}(M_{\rm dyn}/M_\odot) - \log_{10}(M_{\rm baryon}/M_\odot)$ versus the axis ratio, b/a over a range of assumed $(V/\sigma_{V,0})_{R_E}$ values. For each assumed $(V/\sigma_{V,0})_{R_E}$, we calculate the dynamical masses for the galaxies without detected rotation. We then measure the χ^2 between the data and the value if there were no trend with b/a, or a constant $\Delta \log_{10} M$ equal to the median of the $\Delta \log_{10} M$ values. We determine the best-fit $(V/\sigma_{V,0})_{R_E}$ by minimizing the χ^2 statistic.

We find a best-fit $(V/\sigma_{V,0})_{R_E} = 2.1^{+0.2}_{-0.3}$ for the objects without detected rotation. We show the effects of assuming this $(V/\sigma_{V,0})_{R_E}$ value in the right panel of Figure 9. When we adopt $(V/\sigma_{V,0})_{R_E} = 2.1$, we notice very little offset in $\Delta \log_{10} M$ as a function of b/a, and the total scatter in $M_{\rm dyn}$-$M_{\rm baryon}$ is also slightly lower. We note that this measurement reflects an estimate of the typical $(V/\sigma_{V,0})_{R_E}$ of this sample; the scatter in the $M_{\rm dyn}$-$M_{\rm baryon}$ relation also includes variations introduced by a range of intrinsic $(V/\sigma_{V,0})_{R_E}$ values for the sample without observed rotation. The typical $(V/\sigma_{V,0})_{R_E}$ of the galaxies with and without observed rotation are identical, suggesting that on average all galaxies have similar support from random motions.

4.3. *Trends between V/σ and other galaxy properties*

The ratio V/σ is a measure of the amount rotational support versus support from random motions, and thus provides information about the structure of a galaxy. Higher V/σ are indicative of thin disks, while lower V/σ values may indicate thicker disks or high gas turbulence. To understand the physical processes setting the internal structure of star-forming galaxies at $z \sim 2$, we investigate the relation between V/σ and other galaxy properties.

We show the measured $(V/\sigma_{V,0})_{2.2} = V(2.2r_s)/\sigma_{V,0}$ values for our sample of galaxies as a function of Hα specific star formation rate (SSFR) and stellar mass in Figure 10. For the galaxies without observed rotation, we show the median $(V/\sigma_{V,0})_{2.2}$ values in bins of Hα SSFR and stellar mass, calculated using the method described in Section 4.2 and assuming $r_t = 0.4r_s$. For comparison, we also show the KMOS^{3D} results of Wisnioski et al. (2015) at $z = 1$ and $z = 2$ as the grey open triangles and diamonds, respectively. We note

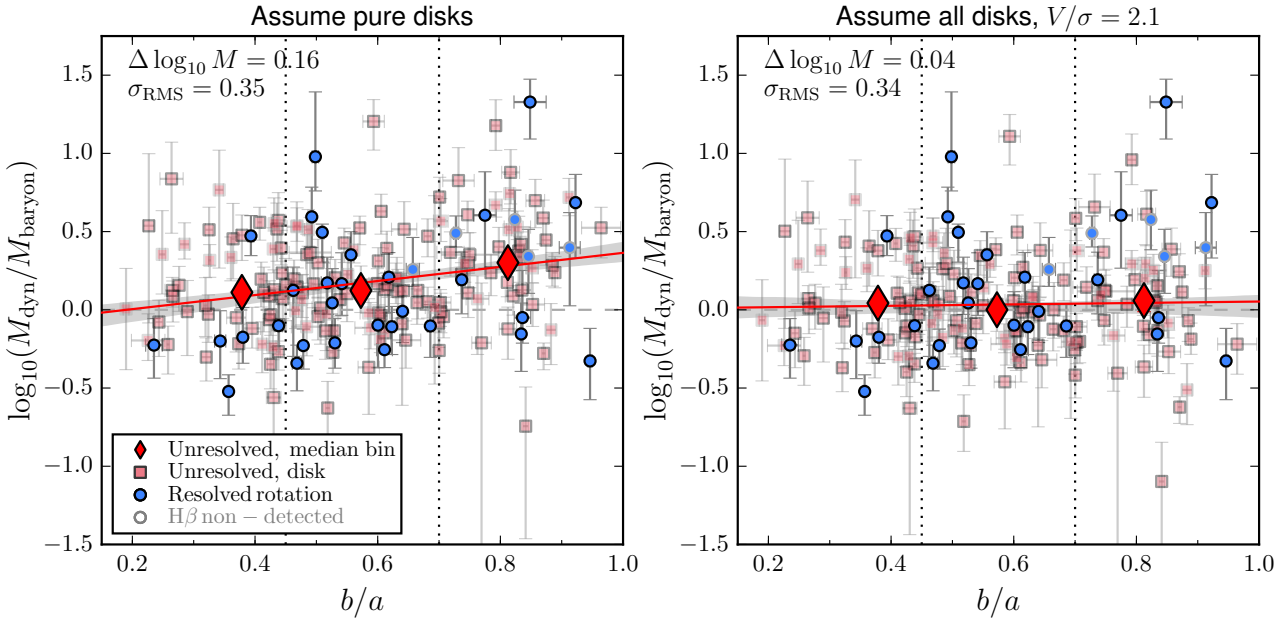

FIG. 9.— The difference between the dynamical and baryonic masses $\Delta \log_{10} M$ vs. axis ratio b/a under different assumptions of $(V/\sigma_{V,0})_{R_E}$. The galaxies with and without detected rotation are shown as blue circles and red squares, respectively. Galaxies without Hβ detections are marked with grey outlines. In the left and right panel, we assume no intrinsic velocity dispersion (i.e., $(V/\sigma_{V,0})_{R_E} \to \infty$) and $(V/\sigma_{V,0})_{R_E} = 2.1$, respectively, for the objects without observed rotation. We show the median values of $\Delta \log_{10} M$ and b/a for the objects without observed rotation within bins of b/a ($[0, 0.45), [0.45, 0.7), [0.7, 1]$) as red diamonds, and show the linear best-fit to the median points as the red line. The bin boundaries are shown as the black dotted lines.

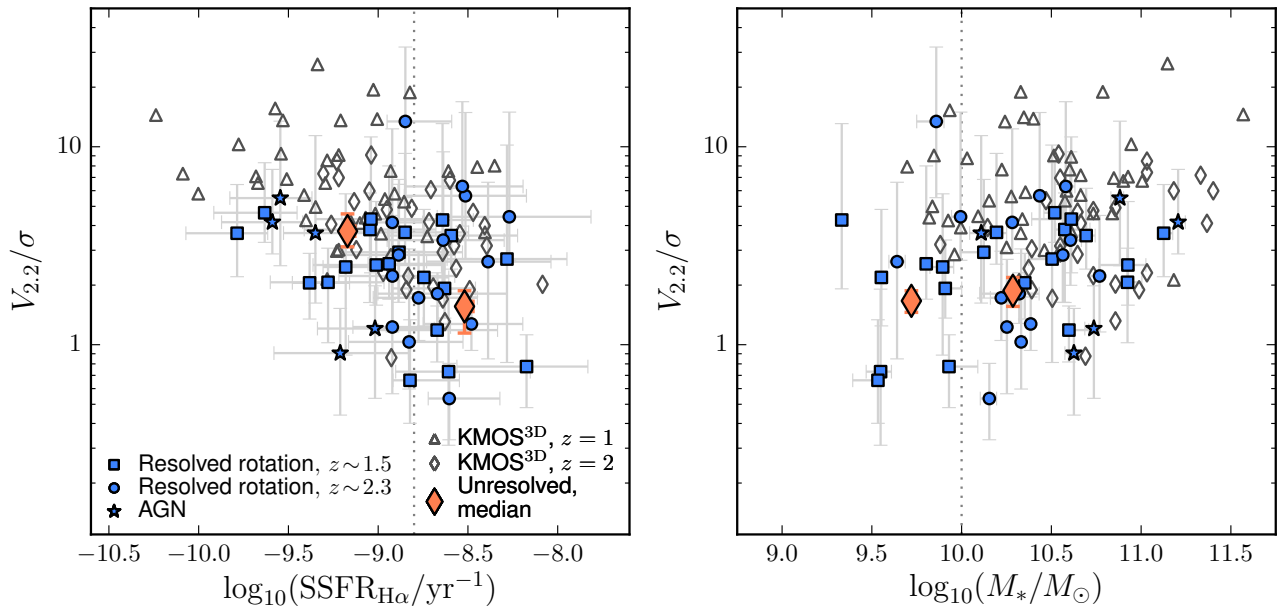

FIG. 10.— The ratio of support from rotation and random motions $(V/\sigma_{V,0})_{2.2}$ vs. Hα SSFR (left panel) and stellar mass (right panel) for our sample of galaxies with detected rotation. Galaxies at $z \sim 1.5$ and $z \sim 2.3$ are shown with blue squares and circles, respectively. We also show the AGN with detected rotation as blue stars. For the galaxies without observed rotation, we show the median $(V/\sigma_{V,0})_{2.2}$ in bins of Hα SSFR and stellar mass (orange diamonds). The bin boundaries are shown by the vertical grey dotted lines. For comparison, we also show the KMOS^{3D} values (Wisnioski et al. 2015) at $z = 1$ and $z = 2$ as the grey open triangles and diamonds, respectively. When considering both our data and the KMOS^{3D} data, there is a trend of decreasing V/σ with increasing SSFR, consistent with the trend found by Wisnioski et al. (2015). This trend may reflect disk settling, with the velocity dispersions decreasing as the gas fractions decrease.

that Wisnioski et al. measure the rotation velocity from the difference between the observed minimum and maximum velocities along the major kinematic axis. However, we do not directly constrain the flat portions of the rotation curves, so instead we consider $V_{2.2} = V(r = 2.2r_s)$ – the radius at which an exponential rotation curve peaks – to attempt to provide a reasonable comparison with existing measurements. We also note that we assume a constant $\sigma_{V,0}$, while Wisnioski et al. measure σ_0 in the outer portions of the galaxies.

We see a trend of decreasing $(V/\sigma_{V,0})_{2.2}$ with increasing Hα SSFR, especially when considering the binned measurement for galaxies without observed rotation and when adding the results by Wisnioski et al. (2015). As suggested by Wisnioski et al. (2015), this trend may reflect disk settling, where galaxies with lower gas fractions (and lower SSFRs) have lower velocity dispersions. For the galaxies without observed rotation, this trend may also reflect a higher fraction of dispersion dominated galaxies at high SSFRs. Our measured $(V/\sigma_{V,0})_{2.2}$ values do not show a trend with stellar mass, but when considering our data together with the results of Wisnioski et al. (2015), we may see a weak trend of increasing V/σ with increasing stellar mass.

When measuring the kinematics, we assume that the velocity dispersion is constant. If the true velocity dispersion profile rises towards the center of a galaxy (as discussed in Section 5.7), our measured $\sigma_{V,0}$ may be systematically higher than what would be measured in the outer portions of our galaxies. This would systematically shift our measured $(V/\sigma_{V,0})_{2.2}$ to lower values than those found by Wisnioski et al. (2015). Thus the trends of V/σ with Hα SSFR and stellar mass found from the combined samples may be partially due to a systematic difference between the adopted V/σ values.

5. DISCUSSION

In this section we analyze how different assumptions and caveats may influence our results. In Section 5.1, we consider the results if instead of baryonic masses we had compared just stellar and dynamical masses. Section 5.2 presents the implications of treating our galaxies as dispersion-dominated galaxies. In Section 5.3, we discuss constraints on the IMF based on our measured $M_{\rm baryon}$ and $M_{\rm dyn}$ values. In Section 5.4, we use our data to investigate the modified $S_{0.5}$ Tully Fisher relation (e.g., Kassin et al. 2007). We compare the $M_{\rm baryon} - M_{\rm dyn}$ relation of the selected AGN to the relation measured for our star-forming galaxy sample in Section 5.5. Section 5.6 examines differences between the stellar continuum and Hα intensity profiles. Finally, we discuss caveats to assumptions we have made in Section 5.7.

5.1. *Importance of including gas in comparisons to dynamical masses*

Previous studies have compared stellar masses to dynamical masses, especially using the stellar kinematics of quiescent galaxies (e.g., Newman et al. 2010, Taylor et al. 2010, Bezanson et al. 2013, van de Sande et al. 2013, Belli et al. 2014). For quiescent galaxies this may be a fair comparison, but for high redshift star-forming galaxies the gas mass is found to be a non-negligible fraction of the total baryonic mass (e.g., Tacconi et al. 2013).

To assess this finding, we consider the difference between the dynamical masses and the stellar masses alone versus Hα SSFR in the left panel of Figure 11. There is an offset between the masses, with the dynamical masses generally exceeding the stellar masses. When we split the sample into bins of Hα SSFR ($\log_{10}({\rm SSFR_{H\alpha}}) < -9.25$, $-9.25 \leq \log_{10}({\rm SSFR_{H\alpha}}) < -8.75$, $\log_{10}({\rm SSFR_{H\alpha}}) \geq -8.75$), we find that the higher SSFR bins have larger offsets between the dynamical and stellar masses than the lower SSFR bins. This result is not surprising, as the median inferred ratios of $f_{\rm gas} = M_{\rm gas}/(M_* + M_{\rm gas})$ are $f_{\rm gas} = 0.22$, $f_{\rm gas} = 0.44$, and $f_{\rm gas} = 0.58$ for the lowest to highest SSFR bins, respectively.

In contrast, the baryonic masses (right panel of Figure 11) show a much weaker SSFR-dependent offset with respect to the dynamical masses. The $M_{\rm dyn}/M_{\rm baryon}$ – SSFR relation also show a smaller observed scatter ($\sigma_{\rm RMS} = 0.34\,{\rm dex}$) than the $M_{\rm dyn}/M_*$ – SSFR relation ($\sigma_{\rm RMS} = 0.37\,{\rm dex}$). The agreement between the baryonic and dynamical masses, as well as the larger $M_{\rm dyn}/M_*$ offset for higher SSFR galaxies, suggests that our Hα SFR-based gas masses are reasonable estimates of the true values.

Thus, at least for star-forming galaxies, it is important to include the gas masses in the total baryonic mass when comparing it against the dynamical masses.

5.2. *What if we assume that all galaxies without detected rotation are early-type galaxies?*

As our sample consists of star-forming galaxies, we have assumed that there is some amount of rotational support for all galaxies, even for those that are not kinematically resolved. However, it might be the case that some, if not all, of these objects without observed rotation are early-type galaxies. To assess this possibility, we derive dynamical masses assuming instead that all the kinematically unresolved galaxies are dispersion-dominated ellipticals or lenticulars (S0s).

We calculate the dynamical masses as

$$M_{\rm dyn} = \beta(n)\frac{\sigma^2_{e,\rm corr} R_{E,\rm circ}}{G}. \quad (5)$$

Here we use the Sérsic index dependent virial coefficient, $\beta(n)$, given in Cappellari et al. (2006), where $\beta(n)$ is a quadratic function of n (e.g., $\beta(n = 1) \sim 8$ and $\beta(n = 4) \sim 6$). The observed integrated velocity dispersions (σ_V) are corrected (to $\sigma_{e,\rm corr}$) using an aperture correction similar to that presented in van de Sande et al. (2013), modified to include the axis ratio and position angle offset relative to the slit. When calculating the dynamical masses, we use the circularized effective radii, $R_{E,\rm circ} = R_E\sqrt{b/a}$, with R_E the GALFIT effective radius (which is equal to the semi-major axis) and b/a the axis ratio. It is necessary to use $R_{E,\rm circ}$ in this case, as $\beta(n)$ is derived using circularized radii. The resulting mass difference $\Delta\log_{10} M$ as a function of axis ratio, b/a, is shown in Figure 12.

Under these assumptions, the dynamical masses are also in reasonable agreement with the baryonic masses ($\Delta\log_{10} M = -0.07\,{\rm dex}$, $\sigma_{\rm RMS} = 0.37\,{\rm dex}$), though the mass offset is somewhat lower than measured for the galaxies with detected rotation. Remarkably, there is no trend of $\Delta\log_{10} M$ with b/a, which is due to the circularization of the effective radii. For objects with smaller axis ratios b/a, the circularized radii will be smaller, and thus the dynamical masses will be lower than if they were calculated using non-circularized radii. Thus, the Sérsic dependent virial coefficient, combined with the circularized radius has a similar effect as the inclination correction applied when assuming that the galaxies are primarily supported by rotation.

The agreement between the dynamical masses for the two

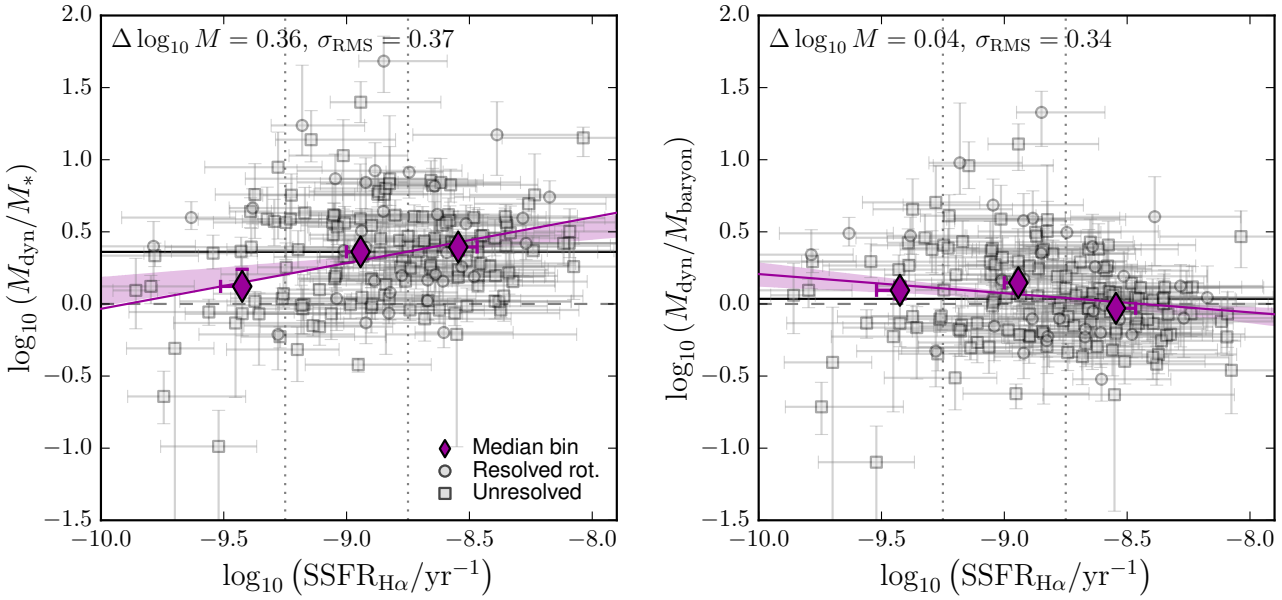

FIG. 11.— Difference between the dynamical and the stellar (left) and baryonic masses (right), versus the Hα SSFR. The objects with observed rotation are shown as circles, and the objects without observed rotation as squares. The median $\Delta(\log_{10} M)$ for the entire sample is shown with the black line. The data are binned in $\mathrm{SSFR_{H\alpha}}$, with the median values shown as the purple diamonds, and a linear fit to the median points is shown with the purple line. In the left panel, we see a larger offset between the dynamical and stellar masses for galaxies with higher SSFR than those with lower SSFR. This offset is reduced when instead we compare the dynamical and baryonic masses. Additionally, the scatter between the mass values is larger when comparing the dynamical and the stellar ($\sigma_{\rm RMS} = 0.37$ dex) rather than the baryonic ($\sigma_{\rm RMS} = 0.34$ dex) masses. This figure illustrates the importance of including gas masses in the mass comparison.

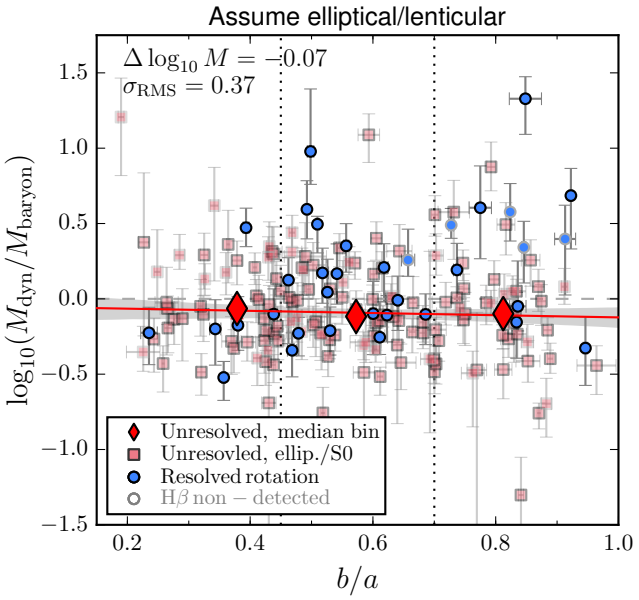

FIG. 12.— The difference between dynamical and baryonic masses vs. axis ratio b/a assuming that the galaxies without observed rotation are ellipticals or lenticulars (S0s). The observed velocity dispersions for the galaxies without apparent rotation are corrected using a modified aperture correction based on the method by van de Sande et al. (2013). The dynamical masses are then calculated using virial coefficient $\beta(n)$ and the circularized effective radii $R_{E,\rm circ}$. The plot point and line definitions are the same as in Figure 9. The Sérsic dependent virial coefficient combined with the circularized radius results in no trend with axis ratio, similar to the effect of applying inclination corrections when assuming the galaxies have partial rotational support.

separate methods may explain why both star-forming and quiescent galaxies, when treated as early-type galaxies, share "one mass fundamental plane," as found by Bezanson et al. (2015). In this work both star-forming and quiescent galaxies fall on the same surface in the 3D parameter space defined by effective radius R_E, velocity dispersion σ_V, and stellar mass surface density Σ_*. We note that when assuming all unresolved galaxies are early-type galaxies, the median offset $\Delta \log_{10} M$ is negative, with the typical galaxy lying in the unphysical regime where $M_{\rm dyn} < M_{\rm baryon}$. This result could suggest that more accurate dynamical masses are obtained when assuming the galaxies are rotationally supported. However, both the baryonic and dynamical masses are subject to systematic uncertainties, and thus we cannot definitively state whether the unresolved galaxies are rotationally supported or not.

5.3. *Stellar initial mass function constraints*

In this section we consider the implications of the measured $M_{\rm baryon}$ and $M_{\rm dyn}$ values of our galaxy sample for the stellar IMF. In estimating the baryonic masses, we have assumed a Chabrier (2003) IMF. An alternative choice is a Salpeter (1955) IMF, which would result in higher stellar masses, by a factor of 1.8 (e.g., Erb et al. 2006). The relations between $L(\mathrm{H}\alpha)$ and SFR, and $\Sigma_{\rm SFR}$ and $\Sigma_{\rm gas}$ given by Kennicutt (1998) both contain an IMF dependence, but the relation between the intrinsic $L(\mathrm{H}\alpha)$ and $\Sigma_{\rm gas}$ does not depend on the IMF, so the gas masses do not change whether using a Salpeter or a Chabrier IMF.

We show the implications of assuming a Salpeter rather than a Chabrier IMF in Figure 13. The median $\log_{10}(M_{\rm dyn}/M_{\rm baryon})$ for the whole sample is shown as the solid black line. If we had instead adopted a Salpeter IMF (right panel), the zero-point of $\log_{10}(M_{\rm dyn}/M_{\rm baryon})$ is lower.

Physically, we expect that the dynamical mass, which traces all mass in a galaxy, must at least be as large as the observed baryonic mass, depending on the dark matter fraction within an effective radius. The median $\log_{10}(M_{\rm dyn}/M_{\rm baryon})$ we

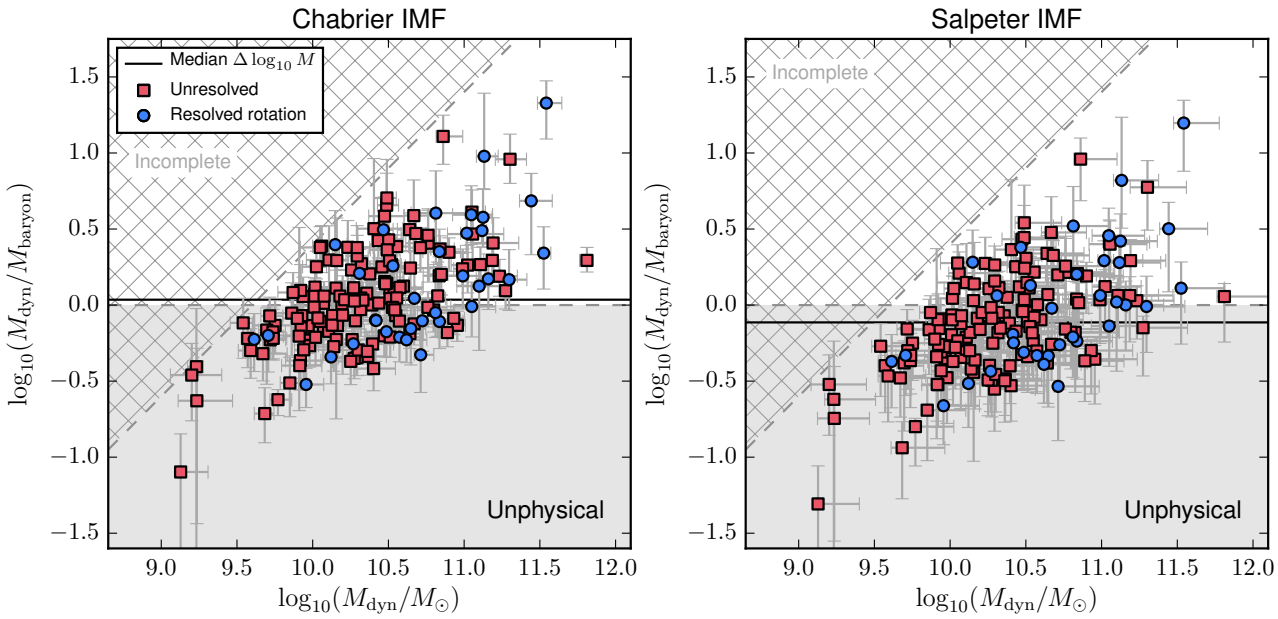

FIG. 13.— $\log_{10}(M_{\rm dyn}/M_{\rm baryon})$ vs. $\log_{10} M_{\rm dyn}$ for a Chabrier (left panel) and a Salpeter IMF (right panel). The galaxies with and without detected rotation are shown with the blue and red points, respectively. In each panel, the zero-point $\log_{10}(M_{\rm dyn}/M_{\rm baryon}) = 0$ is presented by the dotted grey line, and the median $\Delta \log_{10} M = \log_{10}(M_{\rm dyn}/M_{\rm baryon})$ of the whole galaxy sample by the solid black line. The unphysical region where $M_{\rm dyn} < M_{\rm baryon}$ is shaded grey. The mass incomplete region ($M_{\rm baryon} \lesssim 10^{9.6} M_{\odot}$) is shown with the grey hatched region. A Chabrier IMF is consistent with our measurements, while a Salpeter IMF is not; this IMF shifts the median to the region where $M_{\rm dyn} < M_{\rm baryon}$, which is unphysical.

measure assuming a Chabrier IMF is consistent with this expectation, with 46% of the galaxies fall within the unphysical regime. However, for a Salpeter IMF 63% of the galaxies fall within the unphysical regime where $M_{\rm dyn} < M_{\rm baryon}$. Thus a Salpeter IMF is inconsistent with our measured values of $M_{\rm baryon}$ and $M_{\rm dyn}$. This inconsistency with a Salpeter IMF is in agreement with the findings of other studies of star-forming, disk galaxies (Bell & de Jong 2001, Tacconi et al. 2008, Dutton et al. 2011a, Brewer et al. 2012). Nonetheless, our result is subject to potential systematic uncertainties that might decrease the measured dynamical masses, such that our measurements would be inconsistent with both a Salpeter (1955) and a Chabrier (2003) IMF. We discuss these systematic uncertainties in detail in Sections 5.6 and 5.7.

Finally, there is a suggestive trend between $M_{\rm dyn}/M_{\rm baryon}$ and $M_{\rm dyn}$, such that more massive galaxies may have a steeper IMF (or a larger dark matter fraction). However, this trend primarily reflects the cutoff in observed baryonic masses (upper envelope). Thus, at fixed dynamical mass, we miss galaxies with the lower baryonic masses. These missed galaxies could increase the median baryonic-dynamical mass offset, leaving room for more dark matter, or bringing the Salpeter IMF into agreement with our data.

5.4. *Modified stellar mass Tully-Fisher relation*

The Tully-Fisher relation (TFR, Tully & Fisher 1977) - which relates the luminosity of disk galaxies to their rotation velocity - captures information about the interplay between the build-up of disk galaxies and their dark matter halos. As the luminosity-based TFR is subject to luminosity evolution (due to aging populations) and a possible evolution in the gas mass fraction, more recent works have focused on measuring the stellar mass or baryonic mass TFRs, as mass allows for more straight-forward comparisons between redshifts (e.g., Dutton et al. 2011b, Gnerucci et al. 2011, Miller et al. 2012, Vergani et al. 2012).

Furthermore, Kassin et al. (2007) argue that the stellar and baryonic TFRs may evolve due to the increase of non-rotational support in higher redshift galaxies. To account for the increased non-rotational support, they argue for the adoption of the $S_{0.5}$ kinematic indicator, with $S_{0.5} = \sqrt{0.5 V_{\rm rot}^2 + \sigma_V^2}$. This study shows a reduction of scatter in the $S_{0.5}$-M_* TFR relative to the standard M_*-TFR at $z \sim 0.2 - 1$. Furthermore, they find that there is barely any evolution in the $S_{0.5}$-M_* TFR out to $z \sim 1$.

We use our kinematic measurements to examine the $S_{0.5}$-M_* and $S_{0.5}$-$M_{\rm baryon}$ TFRs for our sample of star-forming galaxies at $z \sim 1.5 - 2.6$, shown in Figure 14. We perform a weighted linear fit of $S_{0.5}$ vs M_* (left panel, Figure 14) to our sample of star-forming galaxies by fixing the slope to the average value Kassin et al. (2007) find at $z \sim 0.1 - 1.2$ (i.e., slope $= 0.34$). We find a moderate correlation between $S_{0.5}$ and M_*, with scatter in $S_{0.5}$ of $\sigma_{\rm RMS} = 0.17$ dex for our star-forming galaxies. The scatter is similar to the average scatter Kassin et al. (2007) find (0.16 dex). Our best-fit relation is offset to higher $S_{0.5}$ compared to the average relation found by Kassin et al. (2007) (black dashed line, left panel of Figure 14), which may be explained by lower average gas fractions of star-forming galaxies at lower redshifts. We find a similar intercept if we fit the $S_{0.5} - M_*$ relation using only the galaxies with detected rotation.

We follow the same general method to fit $S_{0.5}$ vs $M_{\rm baryon}$ (right panel, Figure 14), adopting the slope of the $S_{0.5}$-$M_{\rm baryon}$ TFR at $z \sim 0.2$ measured by Kassin et al. (2007) (i.e., slope $= 0.39$), and find a correlation between $S_{0.5}$ and $M_{\rm baryon}$ with a scatter in $S_{0.5}$ of 0.16 dex. Our $S_{0.5}$ intercept is somewhat lower than found by Kassin et al. (2007) at $z \sim 0.2$ (dashed black line, right panel), suggesting an increase in $S_{0.5}$ at fixed $M_{\rm baryon}$ over time. We find the same result if we exclude the galaxies without detected rotation. The

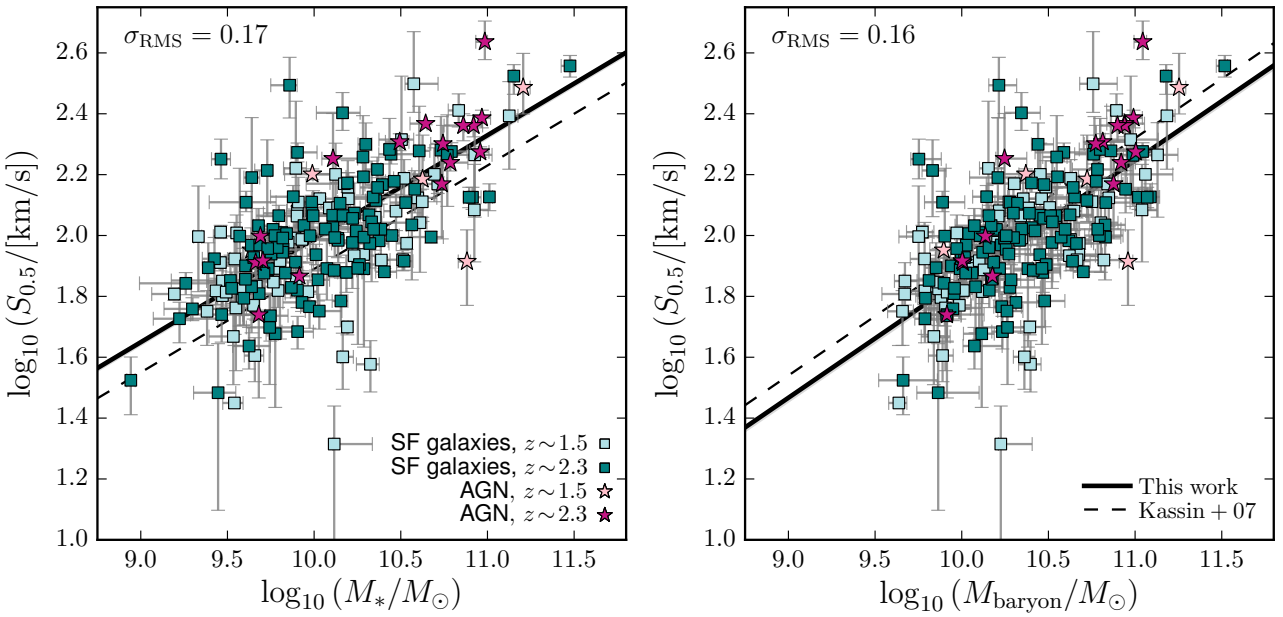

FIG. 14.— The modified $S_{0.5}$-M Tully-Fisher (TF) relation (Kassin et al. 2007) for our sample galaxies with and without detected rotation. The left and right panels show the stellar and baryonic $S_{0.5}$-M TF relations, respectively, with $S_{0.5} = \sqrt{0.5V_{2.2}^2 + \sigma_{V,0}^2}$ for our measurements. In each panel, the star-forming galaxies at $z \sim 1.5$ and ~ 2.3 are shown as light blue and teal squares, respectively, and the AGN at $z \sim 1.5$ and ~ 2.3 are shown as pink and purple stars, respectively. For the same slope of the $S_{0.5} - M_*$ relation, our sample has higher $S_{0.5}$ at fixed M_* than the sample of Kassin et al., which may reflect the trend of a decreasing average gas fraction. For the $S_{0.5} - M_{\rm baryon}$ relation we find that, for the same slope, our sample has lower $S_{0.5}$ at fixed $M_{\rm baryon}$ than the sample of Kassin et al. An increase in the average dark matter fraction over time could explain the higher $S_{0.5}$ values observed by Kassin et al.

offset between $S_{0.5}$ intercepts may be explained by a higher dark matter fraction at later times. This trend may reflect the increasing radii of similar-mass star-forming galaxies with decreasing redshift (e.g., Williams et al. 2010, van der Wel et al. 2014a); as dark matter halo profiles are less concentrated than stellar mass profiles, a larger radius results in a higher dark matter fraction.

Nonetheless, systematic differences may affect the comparison of the $S_{0.5} - M$ TFRs. In particular, the rotation velocities are not measured uniformly, which could introduce systematic offsets. Kassin et al. (2007) use the maximum rotation velocity $V_{\rm max}$ (i.e., the velocity at the flat portion of an arctan rotation curve or at $2.2r_s$ for an exponential disk). Our data do not sample the flat portion of the arctan rotation curve, so we instead adopt $V_{2.2}$ as our velocity measurement, as we have reasonable velocity constraints at this radius. Future work is necessary to quantify the differences between the literature measurements, in order to study the M-TFR evolution over time in a consistent manner.

5.5. *Comparison of baryonic and dynamical masses for AGN*

In this section we consider the kinematics of the AGN that fall within our galaxy sample. Interpreting the kinematics of AGN can be challenging, as the line profiles may have contributions from nuclear emission tracing non-virial motions. Therefore, we did not include the AGN in our analysis so far. Here we assess whether the kinematics may still provide a probe of the host-galaxy structure.

We calculate the stellar, gas, and baryonic masses following the procedure of Section 2.1. We measure the Hα kinematics from the resolved 2D or integrated 1D spectra, and derive dynamical masses following the procedures of Sections 3.1, 3.2, and 3.4. The resulting baryonic and dynamical masses for the AGN, along with those of the galaxy sample, are shown in Figure 15.

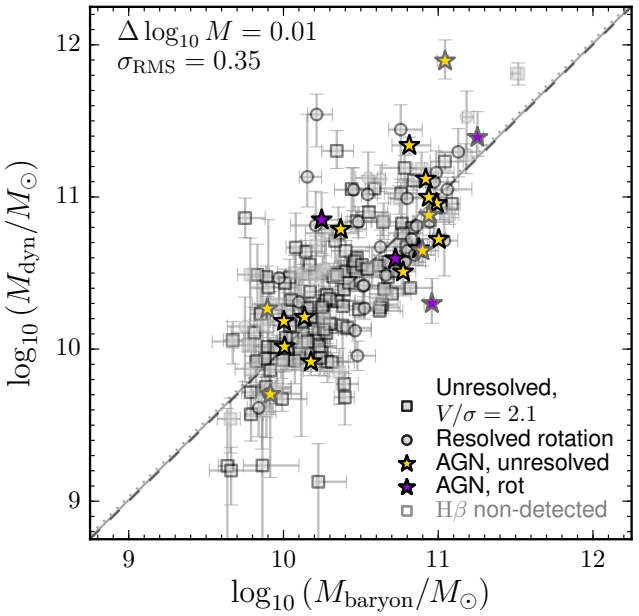

FIG. 15.— $M_{\rm dyn}$ vs. $M_{\rm baryon}$ for the AGN in comparison with the galaxy sample. Galaxies with and without detected rotation galaxies are represented by the grey circles and squares, respectively. The AGN with and without detected rotation are shown with the purple and yellow stars, respectively. The grey line shows the median offset of $\Delta(\log_{10} M) = 0.01$ dex for the AGN, and the dashed grey line shows $M_{\rm dyn} = M_{\rm baryon}$. For reference, the grey dotted line shows the median offset for the star-forming galaxies. The relation between baryonic and dynamical masses for the AGN is similar to the relation for primary galaxy sample, and thus the gas kinematics likely trace the dynamics of the host galaxies.

The AGN that meet our sample selection criteria generally follow the same relation of $M_{\rm dyn} - M_{\rm baryon}$ as the pri-

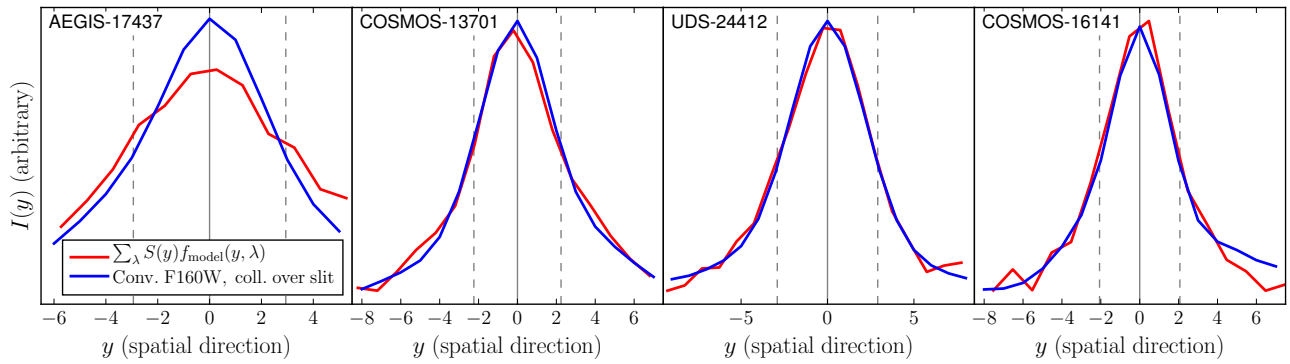

FIG. 16.— Intensity profiles for the stellar continuum and Hα for the four objects shown in Figure 2, with the field and 3D-HST v4 ID noted in the upper left corner of each panel. The normalized stellar light and Hα profiles are shown as the blue and red lines, respectively. The solid grey line shows the emission line center measured during the 1D spectra extraction. The dashed grey lines show the convolved, projected effective radius for each object. The profiles are generally in good agreement, with only the first object having a noticeably larger Hα profile width.

mary galaxy sample. For the AGN we find a median offset $\Delta \log_{10} M = 0.01$ dex, which is slightly lower than the median offset for the star-forming galaxies ($\Delta \log_{10} M = 0.04$ dex), and a scatter of $\sigma_{\rm RMS} = 0.35$ dex. We note that the effective radii may be underestimated for some objects, due to the influence of a nuclear source.

The good agreement between the AGN and galaxies in the $M_{\rm dyn} - M_{\rm baryon}$ plane suggests that the rest-frame optical lines of most AGN in our sample are not dominated by line emission from the nuclear regions, and that we are probing the kinematics of the host galaxies. Our findings support the results of Gabor & Bournaud (2014), who show that in high-resolution hydrodynamic simulations of disk galaxies at $z \sim 2$, AGN have relatively little impact on the gas in galaxy disks.

5.6. *Mass-to-(Hα)-luminosity variations*

When constructing kinematic models, we rely on structural parameters and radii measured from the stellar light distribution, but measure the kinematics from Hα emission. Ideally, we would measure the kinematics from stellar absorption features, but our galaxies are too faint for these measurements. Instead, we assume that the ionized gas and stellar mass have the same distribution and that the gas follows the gravitational potential of the galaxy.

When using kinematic models to measure rotation and interpret the velocity dispersion of unresolved objects, we weight the model velocity field by a luminosity distribution. For the galaxies with detected rotation, this weighting determines the composite velocity profile within a spatial slice, as there is a mix of line-of-sight velocity components, as well as components that fall within the slit, parallel to the spatial direction. The weighting also predicts a light profile along the spatial direction, but our method of fitting the 2D spectra with the models removes this variation in the spatial direction through the scaling factor $S(y)$. For the kinematically unresolved galaxies, the luminosity weighting affects all directions.

To be fully consistent, we should weight the model velocities by the Hα light profile, so there are no mis-matches between the model and observed luminosity profiles. However, the Hα profiles are not well constrained by the MOSDEF data, and most galaxies in our sample lie at redshifts where Hα falls outside of the wavelength coverage of the WFC3 grism (Brammer et al. 2012). We therefore assume that the stellar light profiles are a reasonable approximation for the luminosity weighting. We assess this assumption by comparing the stellar light profiles with the Hα profiles for the galaxies with detected rotation.

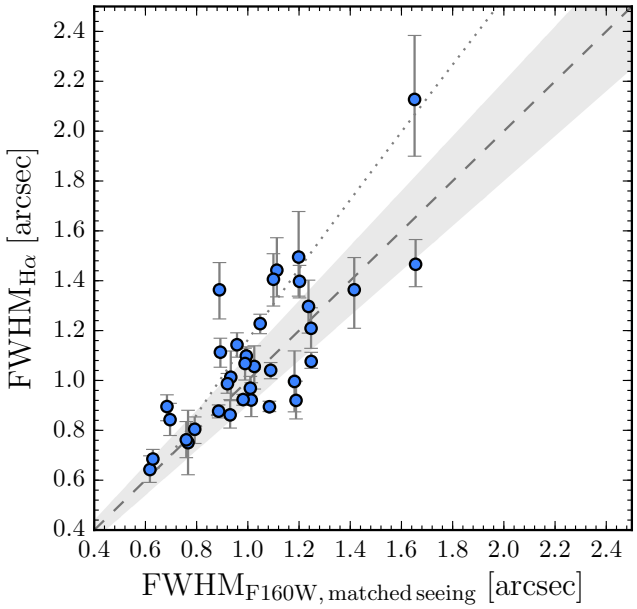

FIG. 17.— $\rm FWHM_{H\alpha}$ vs. $\rm FWHM_{F160W}$ for the galaxies with observed rotation. The Hα FWHM is measured from the scaled 2D emission line model, and the F160W FWHM is measured from the F160W image within the slit, convolved to match the MOSFIRE seeing conditions. The dashed grey line shows the line of equality. The grey shaded region shows the range of values when $\rm FWHM_{H\alpha}$ is 10% smaller or larger than $\rm FWHM_{F160W}$. The FWHMs are similar for most of the galaxies with detected rotation. Also, all but a few of the galaxies lie below the relation $R_{E,\rm H\alpha} = 1.3 R_E$ found by Nelson et al. (2012), with the converted FWHMs convolved with a median seeing FWHM of $\sim 0\farcs7$.

To measure the stellar light profile, we convolve the *HST*/F160W image to match the seeing resolution of the corresponding MOSFIRE spectrum. We then collapse all light falling within the slit along the slit direction. We approximate the Hα profile by collapsing the scaled emission line model, $S(y) f_{\rm model}(y,\lambda)$, over the wavelength direction. We show example F160W and Hα profiles in Figure 16 for the same galaxies shown in Figure 2. For three of the four examples, the stellar and Hα profiles are very similar. Only the first object, AEGIS-17437, has noticeable deviation between the Hα and stellar profiles, where the Hα profile is wider than the stellar light profile.

We quantify the profile differences for all galaxies with de-

tected rotation by fitting the Hα and F160W profiles with Gaussians. We note that the profiles of a number of objects are not well-described by a Gaussian profile, but the FWHM measurements should provide a reasonable, albeit rough, comparison. We compare the widths of the seeing-matched stellar light and Hα profiles in Figure 17. Generally, the FWHMs are in reasonable agreement, and only a few objects have FWHMs that differ by more than 10% (objects lying outside the grey shaded region). Additionally, we show the relation $R_{E,\mathrm{H}\alpha} = 1.3R_E$ found by Nelson et al. (2012) as the dotted grey line, converted to FWHMs and convolved with a median seeing FWHM of $\sim 0\farcs7$. All but a few of the galaxies lie below this line, suggesting that the Hα sizes for our sample are closer to the stellar light sizes than for the Nelson et al. sample. Thus, for most of our objects the stellar light profile is a reasonable substitute for the Hα profile, and hence the measured kinematics will not be biased.

However, for galaxies with more extended Hα, such as AEGIS-17437, we may overestimate the velocity dispersion and possibly the rotation velocity, when assuming the stellar light profile in the model construction. This velocity difference can be explained by the fact that the high velocities at large radii have been down-weighted when using the less extended stellar light instead of the Hα profile. The exact changes in the measured velocity and dispersion velocity from the 2D models depend on the misalignment between the major axis and the slit. If $\Delta\mathrm{PA} = 0$, there is symmetric mixing of velocities at different radii within a spatial slice, and the narrower stellar light profile therefore results in less broadening in the wavelength direction. Additionally, by weighting with the narrower stellar light profile, the composite of the velocity components along the line-of-sight direction also results in less broadening in the wavelength direction. Thus, when $\Delta\mathrm{PA} = 0$ and we weight the velocity fields with the stellar light profile, the measured $V(R_E)$ is the same, and $\sigma_{V,0}$ is larger than we would measure when using the Hα light profile. If a galaxy is misaligned with the slit, the measured $V(R_E)$ using the stellar light profile may also be larger than if we weighted with the Hα profile.

The 1D model for AEGIS-17437 would suffer a greater discrepancy if we would have weighted the velocities of the model with the Hα instead of the stellar light profile. The increased weight at large radii would increase the weighted integrated velocity dispersion of the model within the aperture. Thus the ratio $\sigma_{V,\,\mathrm{model}}/V_{\mathrm{RMS}}(R_E)_{\mathrm{model}}$ is higher for the Hα profile than for the stellar light profile, when using the same underlying rotation curve and assumed $(V/\sigma_{V,0})_{R_E}$. Therefore, the corrected RMS velocity values measured using the stellar light profile overestimate the true values.

An additional question is whether the stellar light sizes correctly probe the characteristic size of the underlying matter density profile. In particular, our current calculations have assumed that half of the total mass is enclosed within the half-light radius. However, the half-mass sizes are on average $\sim 25\%$ smaller than the half-light sizes (Szomoru et al. 2013). If we assume the same intrinsic rotation velocity curve, $V(R_E) > V(r_{1/2,\mathrm{mass}})$, and thus the measured $V(R_E)$ (for the resolved models) and $V_{\mathrm{RMS}}(R_E)$ (for the unresolved models) are larger than the velocities at $r_{1/2,\mathrm{mass}}$. If we assume a constant $\sigma_{V,0}$, this difference implies a lower V/σ. In combination with a smaller R_e, this results in a considerably lower dynamical mass. For example, if $r_{1/2,\mathrm{mass}}$ is 25% lower than R_E (as in Szomoru et al. 2013), then a galaxy with $(V/\sigma_{V,0})_{R_E} = 2.1$ at R_E and $r_t = 0.4r_s = 0.4R_E/1.676$ (following Miller et al. 2011, see Appendix B) has $M_{\mathrm{dyn}}(r_{1/2,\mathrm{mass}})$ which is 31% lower than $M_{\mathrm{dyn}}(R_E)$. When applying the correction found by Szomoru et al. (2013) the dynamical masses decline by 0.16 dex (to $\Delta\log_{10} M = -0.12$ dex) and are inconsistent with both a Chabrier (2003) and a Salpeter (1955) IMF.

We illustrate a lower limit of this systematic variation in the left panel of Figure 18, by approximating the changes of $\Delta\log_{10} M$ caused by varying $r_{1/2,\mathrm{mass}}/R_E$ and using $M_{\mathrm{dyn}} = M_{\mathrm{dyn}}(r_{1/2,\mathrm{mass}})$ (i.e., including variations to the RMS velocity and virial coefficient with the assumption of an arctan curve with $(V/\sigma_{V,0})_{R_E} = 2.1$ and $r_t = 0.4r_s = 0.4R_E/1.676$). Even $\sim 10\%$ changes in $r_{1/2,\mathrm{mass}}/R_E$ result in a $\sim 10\%$ change to the inferred dark matter fraction. However, if we instead assume a decreasing velocity dispersion with increasing radius, as we discuss in the next section, the $V_{\mathrm{RMS}}(r_{1/2,\mathrm{mass}})$ values would be larger. This moves in the opposite direction as the above trend, and may change the masses so they remain consistent with a Chabrier (2003) IMF.

5.7. *Other caveats*

In this section we consider caveats to assumptions made in the preceding analysis. Specifically, we focus on possible variations due to assumptions about the accuracy of the structural parameters, misalignment of the photometric and kinematic major axes, the intrinsic thickness of galaxy disks, the accuracy of our derived gas masses, the shape of the rotation curve, and the velocity dispersion profile being constant.

First, we have not fully accounted for the accuracy of the GALFIT-derived structural parameters. We depend on the structural parameters to model the kinematics of the detected rotation curves, to correct the kinematics from integrated 1D spectra, and to calculate the dynamical masses. We include estimated errors on the effective radii when calculating the dynamical masses, but do not include any errors when fitting the kinematic models. Thus, uncertainties in the structural parameters introduce scatter in our derived dynamical masses.

Second, for objects where the photometric and kinematic major axes are misaligned, the inferred velocities and dispersion velocities will be incorrect. If the true $\Delta\mathrm{PA}$ is closer to aligned, the corrected RMS velocities will be over-estimated, while if it is more misaligned, the velocities will be underestimated (as seen in the first panel in Figure 23). We expect similar over- and under-estimates in the measured velocities and dispersions for the galaxies with detected rotation. Additional misalignment uncertainties are introduced by slit alignment issues, which introduce the same trends as stated above.

Third, we assume an intrinsic disk thickness of $(b/a)_0 = 0.19$ to estimate inclination angles. If a galaxy is intrinsically thicker than the assumed value, the inferred inclination angle underestimates the true value. In this case, the inferred intrinsic rotation velocity and $(V/\sigma_{V,0})_{R_E}$ would be overestimated. If a galaxy is thinner, the inclination angle will be overestimated, producing an underestimate of both the rotation and $(V/\sigma_{V,0})_{R_E}$. Thus, variations in disk thickness within our sample will add scatter and a possible systematic offset in our dynamical masses.

Fourth, we assume that the galaxies in our sample follow the SFR-gas mass relation of Kennicutt (1998) for star-forming galaxies in the local universe. Based on a local sample of normal and starburst galaxies, Kennicutt (1998) measure $N = 1.4$ for $\Sigma_{\mathrm{SFR}} \propto \Sigma_{\mathrm{gas}}^N$, where Σ_{gas} includes both

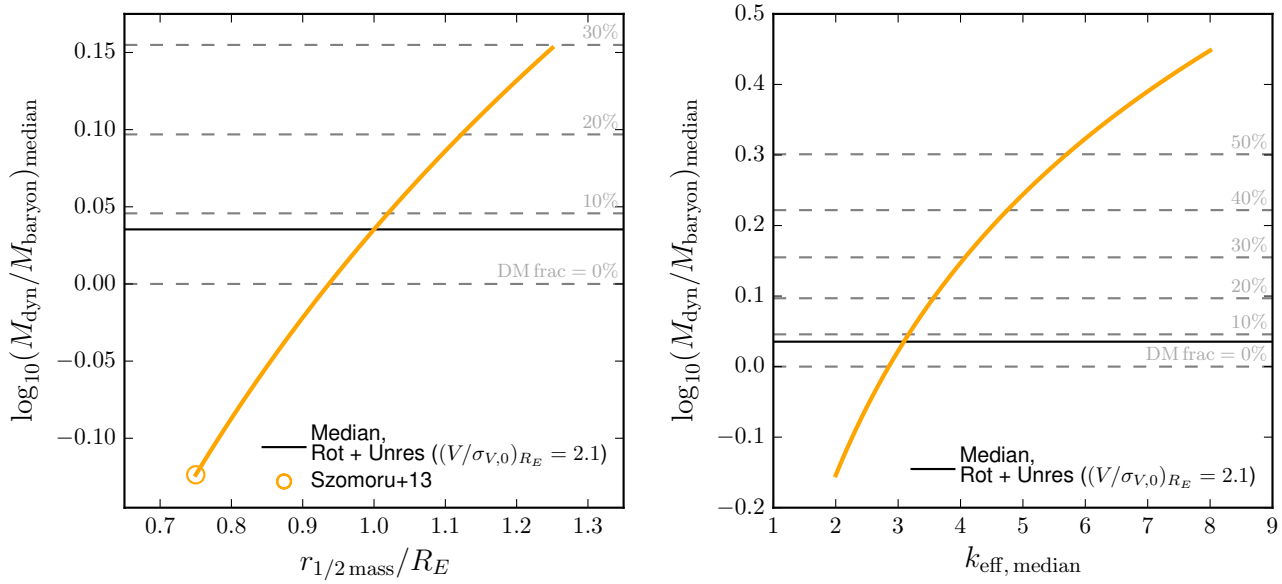

FIG. 18.— Systematic changes in the median $\log_{10}(M_{\rm dyn}/M_{\rm baryon}) = \Delta\log_{10} M$ with varying half-mass to half-light radius ratio ($r_{1/2\,\rm mass}/R_{E,*}$, left panel) and effective virial coefficient ($k_{\rm eff,\,median}$, right panel). In both panels the black horizontal line shows the median $\Delta\log_{10} M$ for the whole sample when adopting the default assumptions. Lines of constant dark matter fraction (assuming $f_{\rm DM} = M_{\rm DM}/M_{\rm dyn} = (M_{\rm dyn} - M_{\rm baryon})/M_{\rm dyn}$) are shown with grey dashed lines. In the left panel, the systematic changes with half-mass to half-light radius ratio include variations of the RMS velocity and virial coefficient assuming an arctan rotation curve with $(V/\sigma_{V,0})_{R_E} = 2.1$ and $r_t = 0.4R_E/1.676$. Szomoru et al. (2013) find that $r_{1/2\,\rm mass}$ is on average 25% lower than R_E (orange circle), which corresponds to the median offset $\Delta\log_{10} M$ shifted to the unphysical region, or $\Delta\log_{10} M \sim -0.12$ dex. In the right panel, the systematic changes with the effective virial coefficient are approximated by applying the same $k_{\rm eff,\,median}$ to all galaxies and calculating the resulting median offset $\Delta\log_{10} M$. Assuming $k_{\rm eff,\,median} \sim k_{\rm rot} = 2.66$ for all galaxies (without changing the assumed $(V/\sigma_{V,0})_{R_E}$) results in an unphysical $\Delta\log_{10} M < 0$, while assuming $k_{\rm eff,\,median} \sim k_{\rm disp} = 5$ results in a much higher inferred dark matter fraction of $f_{\rm DM} \sim 45\%$.

atomic and molecular gas. Analysis of galaxies at $z \sim 1-3$ find slopes that vary between $N = 1.28$ (Genzel et al. 2010) and $N = 1.7$ (Bouché et al. 2007). These values bracket the local slope, so our gas masses may be reasonable. However, if the true slope is lower than the local relation, our gas masses underestimate the true value, while a higher slope implies our gas masses overestimate the true value. An alternate method would be to adopt the gas mass scaling relations presented in Genzel et al. (2015), which relate the gas mass to the stellar mass, the offset from the star-forming main sequence, and the redshift. If we adopt this scaling relation, we see an offset $\Delta\log_{10} M = -0.12$ dex and a scatter of $\sigma_{\rm RMS} = 0.368$ dex between the dynamical and baryonic masses, with the median mass difference lying in the unphysical region where $M_{\rm baryon} > M_{\rm dyn}$. However, the gas mass scaling relations of Genzel et al. (2015) were calibrated for UV+IR SFRs, while we use Hα SFRs in this work. Mismatches between these SFR indicators could be causing the large (~ 0.2 dex) difference between the inferred baryonic masses when using the scaling relation method and the inverted Kennicutt-Schmidt relation. As Kennicutt (1998) calibrated the $\Sigma_{\rm SFR} - \Sigma_{\rm gas}$ relation using Hα SFRs, we opt to estimate the gas masses following this prescription.

Fifth, we have assumed that the rotation velocity profiles of our disk galaxies are well described by arctan models, as shown by Courteau (1997), Weiner et al. (2006), and Miller et al. (2011). Some distant star-forming galaxies exhibit rotation following a Freeman exponential disk model (Freeman 1970), as found by Wisnioski et al. (2015), while van Dokkum et al. (2015) find indications of Keplerian rotation in compact star-forming galaxies. However, preliminary analysis suggests that using an exponential disk rotation curve with our modeling produces poor fits to some of our galaxies. More detailed modeling is required to determine in detail whether an alternative rotation profile provides better agreement with our data and to assess the uncertainties introduced by this assumption.

Sixth, we have assumed that the intrinsic velocity dispersion is constant over all radii. However, the true velocity distribution may decrease with increasing radius, as seen in Genzel et al. (2014) and Wisnioski et al. (2015). For the unresolved objects, a decreasing velocity dispersion distribution would produce higher model RMS velocities for a given $(V/\sigma_{V,0})_{R_E}$ measured at R_E,[2] as matching the same $\sigma_V(R_E) \approx \sigma_{V,0}$ implies a higher central velocity dispersion, $\sigma_V(r=0)$. A velocity dispersion profile which rises towards the center would increase the integrated model velocity dispersions but not the model RMS velocity at R_E, leading to lower corrected RMS velocities and lower dynamical masses. The trend of decreasing integrated RMS velocity with increasing inclination will also be less strong for a fixed $(V/\sigma_{V,0})_{R_E}$ than with a constant $\sigma_{V,0}$. The median $(V/\sigma_{V,0})_{R_E}$ required to remove the $\Delta\log_{10} M$ trend for the kinematically unresolved galaxies will therefore be higher, increasing the implied amount of rotational support relative to the random motions, which would indicate more settled or thinner disks. Preliminary calculations assuming an additional dispersion term that rises towards the center of a galaxy confirms these general trends, but more careful analysis is necessary to determine the

[2] Other studies (e.g., Newman et al. 2013, Wisnioski et al. 2015) measure $\sigma_{V,0}$ in the outer portions of a galaxy, so taking $\sigma_V(R_E) \approx \sigma_{V,0}$ in the case of a non-constant velocity profile should be a reasonable comparison, though may be higher than the true value depending on the exact form of the additional velocity dispersion term. This notation is in contrast to velocity dispersions of elliptical galaxies, where the *central* velocity dispersions are often denoted as σ_0 or $\sigma_{V,0}$.

correct form of a rising velocity dispersion profile.

Seventh, in our derivation of the dynamical masses we have not included the systematic uncertainties arising from the choice of virial coefficients, $k_{\rm disp}$ and $k_{\rm rot}$. The matter distributions assumed when deriving the virial coefficients may not match the underlying profiles of the star-forming galaxies in our sample, but more detailed analysis is required to quantify the uncertainties introduced by the adopted virial coefficients. We note that the systematic shifts from a different choice of virial coefficient can be non-negligible, and have implications especially for the IMF constraints. For instance, the combination of $k_{\rm disp} = \beta(n)$ (from Cappellari et al. (2006)), $n = 1$, and $(V/\sigma_{V,0})_{R_E} = 2.1$ would have resulted in dynamical masses that are larger by ~ 0.07 dex and an inferred dark matter fraction of $f_{\rm DM} \sim 22\%$. We approximate the systematic changes due to changing only the combined $k_{\rm eff,\,median}$ in the right panel of Figure 18. In this plot, we see that if we assume $k_{\rm eff,\,median} \sim k_{\rm rot} = 2.66$ for all galaxies (without changing the conversion from the integrated velocity dispersions to the RMS velocities for the unresolved galaxies), then the median $\Delta \log_{10} M < 0$, which lies in the unphysical region where $M_{\rm dyn} < M_{\rm baryon}$. If we instead assume $k_{\rm eff,\,median} \sim k_{\rm disp} = 5$ (again with no other changes), we would instead infer a much higher dark matter fraction of $f_{\rm DM} \sim 45\%$ rather than the 8% measured from the default assumptions.

6. SUMMARY

In this paper, we use spectra from the MOSDEF survey to study the masses and kinematic structures of a sample of 178 star-forming galaxies at $1.4 \leq z \leq 2.6$. For all galaxies, structural parameters from CANDELS *HST*/F160W imaging, stellar masses from multi-wavelength photometry, and gas masses from dust-corrected Hα SFRs and the relation by Kennicutt (1998) are available. The gas kinematics have been measured from the Hα emission lines: for 35 of the galaxies we detect resolved rotation, while in the remaining 143 galaxies we only measure the velocity dispersion.

As our galaxies are observed with random orientations compared to the slit angle, we may not see rotation for some objects that are intrinsically rotating. Additionally, we may not resolve rotation due to seeing limitations, as found by Newman et al. (2013). To estimate how many of our galaxies are consistent with rotation, we compare the projected Hα major axis size within the slit to the seeing and use this to estimate whether a galaxy is spatially resolved or not. The majority of our sample (80%) is too small relative to our seeing, and thus these galaxies may indeed be unresolved rotating disks.

We have developed models to convert the observed kinematic measurements into intrinsic rotation and dispersion velocities. These models use the sizes, Sérsic indices, axis ratios, and position angles measured from the F160W imaging to simultaneously account for the inclination of the galaxy, the misalignment of photometric major axis and the slit, and determine which portions of the galaxy fall within the slit. In the case of galaxies with detected rotation, we directly constrain $V(R_E)$ and $\sigma_{V,0}$, and find a median $[(V/\sigma_{V,0})_{R_E}]_{\rm 2D,median} = 2.1$. For the galaxies without observed rotation, the models allow us to convert the observed velocity dispersion into an RMS velocity for an assumed ratio of $(V/\sigma_{V,0})_{R_E}$.

When assuming that the galaxies with and without detected rotation have a similar V/σ, we find that the baryonic ($M_{\rm baryon} = M_* + M_{\rm gas}$) and dynamical masses of the total sample are in good agreement, with a median offset of $\Delta(\log_{10} M) = 0.04$ dex and a scatter of $\sigma_{\rm RMS} = 0.34$ dex. Moreover, we directly constrain the mean $(V/\sigma_{V,0})_{R_E}$ for the galaxies without detected rotation by removing any trend of $\log_{10}(M_{\rm dyn}/M_{\rm baryon})$ with axis ratio b/a and find $[(V/\sigma_{V,0})_{R_E}]_{\rm 1D,median} = 2.1^{+0.2}_{-0.3}$. The offset between the dynamical and baryonic masses implies a dark matter fraction within R_E of 8% for a Chabrier (2003) IMF, which is lower than the value measured within $2.2r_s$ for local star-forming galaxies (Pizagno et al. 2005; Dutton et al. 2011a) or within $r < 10$ kpc for galaxies at $z \sim 2$ (Förster Schreiber et al. 2009).

The consistency between the dynamical and baryonic masses relies on the inclusion of gas masses. When comparing the dynamical masses with only stellar masses, we find a larger scatter ($\sigma_{\rm RMS} = 0.37$ dex). Furthermore, the median offset between the stellar and dynamical mass increases with increasing Hα SSFR, which is suggestive of a larger gas fraction at higher SSFRs.

We examine trends in the ratio of support from rotation and random motions, V/σ, as a function of Hα SSFR and stellar mass. For galaxies without detected rotation, we bin by Hα SSFR and stellar mass and estimate V/σ by removing any variation of $\log_{10}(M_{\rm dyn}/M_{\rm baryon})$ with axis ratio. We see a trend of decreasing V/σ with increasing Hα SSFR and a possible weak trend of increasing V/σ with increasing stellar mass when combining our measurements with the sample by Wisnioski et al. (2015). The trend of decreasing V/σ with increasing Hα SSFR may reflect disk settling, such that galaxies with lower SSFRs have lower gas fractions and therefore lower velocity dispersions.

While our assumption that all galaxies without detected rotation are disks results in highly consistent dynamical and baryonic masses, we also find a strong correspondence between the two masses if we had instead assumed that all unresolved galaxies are dispersion dominated. Differences in the methods of calculating the dynamical masses (i.e., using circularized radii for early-type galaxies vs. inclination corrections for disks, different virial coefficients) may explain why the dynamical masses are so similar, and why there is no observed trend of $\log_{10}(M_{\rm dyn}/M_{\rm baryon})$ with axis ratio.

The measured masses also provide insight into the stellar IMF in $z \sim 2$ star-forming galaxies. The baryonic and dynamical masses of our sample are consistent with a Chabrier (2003) IMF. A Salpeter (1955) IMF is disfavored by our data, as it would lead to baryonic masses that exceed the dynamical masses by ~ 0.1 dex on average. However, when assuming that the half-mass sizes are 25% smaller than the half-light sizes (Szomoru et al. 2013), the inferred masses are also inconsistent with a Chabrier (2003) IMF. Nonetheless, other systematic uncertainties, as discussed in detail in the discussion section, may reduce this mass difference.

We examine the modified $S_{0.5}$-M_* and $S_{0.5}$-$M_{\rm baryon}$ Tully Fisher relations (TFRs) for our sample of galaxies, with $S_{0.5} = \sqrt{0.5V_{2.2}^2 + \sigma_{V,0}^2}$. We find a higher intercept of $S_{0.5}$ than Kassin et al. (2007) measure for the average $S_{0.5} - M_*$ TFR at $z \sim 0.1 - 1.2$, which may be caused by a decrease in the average gas fraction of star-forming galaxies with time. For the $S_{0.5} - M_{\rm baryon}$ TFR, we measure a lower intercept than Kassin et al. (2007) find at $z \sim 0.2$. The change in the $M_{\rm baryon}$-TFR may reflect an increase in the average dark matter fraction with time, possibly caused by the increase in

average galaxy size at fixed mass with decreasing redshift.

Our sample also contains 21 AGN, selected by either X-ray luminosity, IRAC colors, or optical line ratios. As the line emission may be associated with nuclear accretion activity, the broadening may not only probe the kinematics of the host galaxy. We measure the baryonic and dynamical masses for the AGN in our sample, and find that they follow the same trend as the star-forming galaxies. This finding suggests that on average the line profiles do indeed reflect the host galaxy kinematics.

This paper demonstrates the power of using large samples of galaxies observed with multi-object near-infrared spectrographs under seeing-limited conditions to study the average kinematic properties of high redshift galaxies. In particular, combining such observations with high-resolution imaging makes it possible to model the effects of axis misalignment, seeing, and velocity rotation and dispersion on the observed spectra. This technique will prove useful in future studies of galaxy kinematics with *JWST*/NIRSPEC, as this multi-object spectrograph will also suffer from random orientation of galaxies within the slits. Measurements from seeing-limited multi-object spectrographs are not sufficient to constrain kinematic properties of individual high-redshift galaxies, and need to be complimented by adaptive-optics assisted IFU observations. Together, these approaches will provide a powerful probe of the nature of galaxies at this key period of structure formation.

We acknowledge valuable discussions with J. van de Sande, R. Feldmann, P. van Dokkum, M. Franx, R. Genzel, N. Förster-Schreiber, E. Toloba, M. George, and I. Shivvers. We thank the anonymous referee for constructive comments, which have improved this paper. We thank the MOSFIRE instrument team for building this powerful instrument, and for taking data for us during their commissioning runs. We are grateful to M. Kassis at the Keck Observatory for his many valuable contributions to the execution of this survey, and to I. McLean, K. Kulas, and G. Mace for taking observations for us in May and June 2013. This work would not have been possible without the 3D-HST collaboration, who provided us with the spectroscopic and photometric catalogs used to select the MOSDEF targets and derive stellar population parameters. We acknowledge support for the MOSDEF survey from NSF AAG collaborative grants AST-1312780, 1312547, 1312764, and 1313171, and archival grant AR-13907, provided by NASA through a grant from the Space Telescope Science Institute. SHP acknowledges support from the National Science Foundation Graduate Research Fellowship under grant DGE 1106400. MK acknowledges support from the Hellman Fellows fund. ALC acknowledges funding from NSF CAREER grant AST-1055081. NAR is supported by an Alfred P. Sloan Research Fellowship. The data presented in this paper were obtained at the W. M. Keck Observatory, which is operated as a scientific partnership among the California Institute of Technology, the University of California, and the National Aeronautics and Space Administration. The Observatory was made possible by the generous financial support of the W. M. Keck Foundation. The authors wish to recognize and acknowledge the very significant cultural role and reverence that the summit of Mauna Kea has always had within the indigenous Hawaiian community. We are most fortunate to have the opportunity to conduct observations from this mountain. This work is also based on observations made with the NASA/ESA Hubble Space Telescope, which is operated by the Association of Universities for Research in Astronomy, Inc., under NASA contract NAS 5-26555. Observations associated with the following GO and GTO programs were used: 12063, 12440, 12442, 12443, 12444, 12445, 12060, 12061, 12062, 12064 (PI: Faber); 12177 and 12328 (PI: van Dokkum); 12461 and 12099 (PI: Riess); 11600 (PI: Weiner); 9425 and 9583 (PI: Giavalisco); 12190 (PI: Koekemoer); 11359 and 11360 (PI: O'Connell); 11563 (PI: Illingworth).

APPENDIX

APPENDIX A: MODELING OF ROTATION IN RESOLVED DISK GALAXIES

Kinematic model definition

The multiplexing capabilities of MOSFIRE, which allow us to study many galaxies simultaneously, come at the price of not observing the galaxies along the kinematic major axis. Misalignment of the kinematic major and slit axes poses problems for the interpretation of kinematic measurements even for resolved disk galaxies. Issues to address include: How much kinematic information is lost because portions of the galaxy fall outside the slit? How much of the line broadening in a spatial row is caused by intrinsic velocity dispersion, and how much is caused by the inclusion of multiple line-of-sight velocities in that slice of the galaxy?

In this appendix, we describe how we model the internal kinematics of a disk galaxy, apply the appropriate inclination and position angle offset to the model, and then collapse the model along the line-of-sight and slit direction to calculate the observed kinematic signature of the object as a function of position along the slit.

To model an ideal disk galaxy with an arbitrary position angle offset with respect to the slit, we define coordinates as shown in Figure 19. First, we consider a point on the galaxy at $(x_{\rm int}, y_{\rm int}, z_{\rm int})$, with distance in the plane of the disk of

$$r_{\rm int} = \sqrt{x_{\rm int}^2 + y_{\rm int}^2} \tag{A1}$$

from the axis of rotation, and define the angle ψ as

$$\cos\psi = y_{\rm int}/r_{\rm int}, \tag{A2}$$

which is the counterclockwise angle between the major axis $\hat{y}_{\rm int}$ and $(x_{\rm int}, y_{\rm int}, z_{\rm int})$ with respect to the rotation axis (see the left panel of Figure 19). We incline our galaxy model by rotating around the major axis $\hat{y}_{\rm int}$. The inclination angle i is estimated as

$$\sin i = \sqrt{\frac{1-(b/a)^2}{1-(b/a)_0^2}}, \tag{A3}$$

where a and b are semi-major and semi-minor axes lengths, respectively, from the GALFIT parameterization. We assume an intrinsic disk axis ratio of $(b/a)_0 = 0.19$ (Miller et al. 2011). By inclining the model (see the middle panel of Figure 19), the intrinsic coordinates are mapped to projected coordinates by

$$\begin{aligned} x_p &= x_{\rm int}\cos i + z_{\rm int}\sin i \\ y_p &= y_{\rm int} \\ z_p &= -x_{\rm int}\sin i + z_{\rm int}\cos i. \end{aligned} \tag{A4}$$

Finally, we apply the position angle offset, ΔPA, between the galaxy major axis and the slit. We rotate the projected

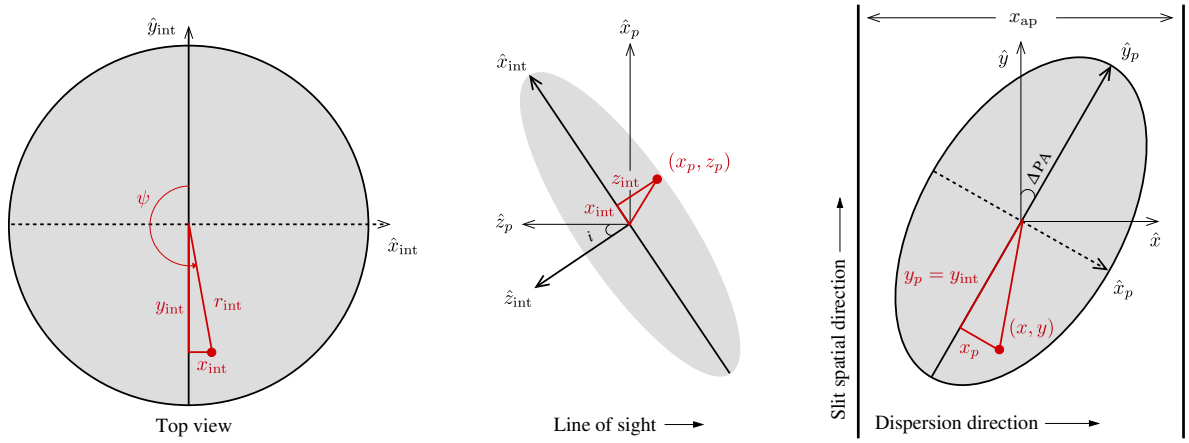

FIG. 19.— Coordinate definition for an inclined disk galaxy misaligned with the slit axis. The left panel shows a top down view of the disk galaxy, depicting the $\hat{x}_{\rm int} - \hat{y}_{\rm int}$ plane, and the definition of $r_{\rm int}$ and the angle ψ. The center panel shows a side view of the inclined disk galaxy, with the line of sight extending to the right. Here we show the coordinate transformation due to inclination from the intrinsic $(x_{\rm int}, z_{\rm int})$ coordinates to the projected (x_p, z_p). The right panel shows the disk galaxy relative to the slit, including the position angle misalignment (ΔPA). The projected coordinates (x_p, y_p) are shown relative to the slit coordinates (x, y).

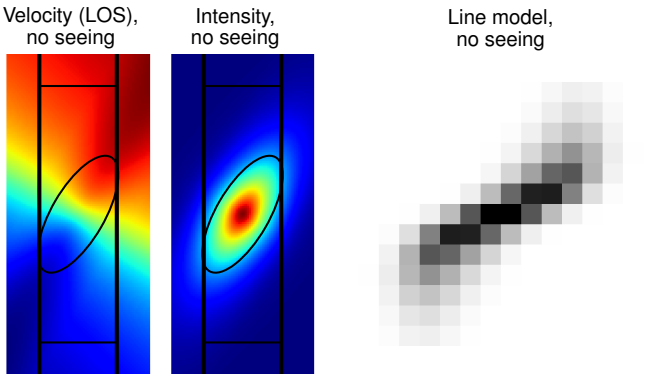

FIG. 20.— Example of the line of sight (LOS) velocity field $V_{\rm obs}(x, y)$ collapsed along the LOS, z (left panel), assumed model intensity collapsed along z, $I(x, y) = \sum_z I(x, y, z)\Delta z$ (center panel), and final composite Hα emission line model (right panel) for a disk. The model shown has $\sigma_{V,0} = 0$, $R_E = 0\farcs6$, $b/a = 0.4$, $n = 1$, ΔPA $= 30°$, $V_a = 200$ km/s, and $r_t = 0.4 r_s = 0.4(R_E/1.676)$. Here we ignore any seeing effects, assuming FWHM$_{\rm seeing} = 0\farcs$, and use a typical instrumental resolution width in calculating the Hα line model. The wide black lines show the slit width, $0\farcs7$, and the horizontal lines show the spatial aperture extent.

model by ΔPA in the $\hat{x}_p - \hat{y}_p$ plane, mapping the projected coordinates into observed coordinates relative to the slit layout (see the right panel of Figure 19) by

$$\begin{aligned} x &= x_p \cos\Delta\mathrm{PA} + y_p \sin\Delta\mathrm{PA} \\ y &= -x_p \sin\Delta\mathrm{PA} + y_p \cos\Delta\mathrm{PA} + y_0 \\ z &= z_p, \end{aligned} \tag{A5}$$

where we also allow for an offset of the object center relative to the slit center in the $\hat{y}$ direction, through the parameter y_0. If we invert this set of coordinate transformations, we may calculate the intrinsic position $(x_{\rm int}, y_{\rm int}, z_{\rm int})$ and intrinsic radius $r_{\rm int}$ within the galaxy for any given point (x, y, z) in the slit coordinate system (see Figure 19, right panel).

To model the kinematics of a disk galaxy, we adopt the arctan model for rotation in exponential disks (Courteau 1997, Miller et al. 2011),

$$V(r, r_t, V_a) = \frac{2}{\pi} V_a \arctan\left(\frac{r}{r_t}\right), \tag{A6}$$

where V_a is the asymptotic velocity and r_t is the turnover radius, which encodes a transition between the rising and flat parts of the rotation curve (Courteau 1997).

We must account for LOS velocity reductions due to projection effects. First, the inclination reduces the LOS velocity by a factor of $\sin i$. The LOS velocity is also reduced by $\cos\psi$, which accounts for the position of every point around the rotational axis of the galaxy. Together, the LOS velocity at each point (x, y, z) is

$$V_{\rm los}(x, y, z) = V(r, r_t, V_a) \cdot \sin i \cdot \cos\psi, \tag{A7}$$

where $r = r_{\rm int}$ and $\cos\psi$ are evaluated given the slit coordinates (x, y, z). We assume the rotation is independent of $z_{\rm int}$, so the model consists of nested cylindrical shells of varying radii, with each shell rotating at the appropriate velocity. We show an example LOS velocity field of a galaxy, integrated along the line-of-sight, in the left panel of Figure 20.

However, our galaxies may not be ideal disks. Thus the galaxies may also have an intrinsic velocity dispersion component, as is the case with thickened disks. We assume the intrinsic dispersion component $\sigma_{V,0}$ is constant over the whole disk, or $\sigma(r) = \sigma_{V,0}$.

The composite kinematic profile of our model, as would be observed with slit spectroscopy, consists of the combination of all the kinematic information of the portions of the galaxy lying within each slit pixel. The relative weights of the individual kinematic components are determined by the associated intensities. Thus we must consider the light distribution of our galaxy model. We assume that the light follows a modified Sérsic intensity profile,

$$I(r, n, R_E, z_{\rm int}) = \tag{A8}$$
$$I_e \exp\left\{-b_n\left[\left(\frac{r}{R_E}\right)^{1/n} - 1\right]\right\} \exp\left[-\frac{z_{\rm int}}{q_0 R_E}\right],$$

where n and R_E are set to the GALFIT best-fit parameters, $b_n \approx 2n - 0.324$ (Ciotti & Bertin 1999), and approximating the vertical scale height as $z_0 = q_0 R_E$. We show a simple example intensity profile, integrated over the line-of-sight, in the center panel of Figure 20.

The composite 2D line model is constructed by combining the line-of-sight velocity information and the assumed

intensity profile. We begin by calculating the intensity $I(x,y,z)$ and observed velocity $V_{\rm los}(x,y,z)$ at every point in our slit coordinates. To include the velocity dispersion, $\sigma_v(x,y,z)$, we assume that at every point (x,y,z) the intensity has a gaussian distribution with wavelength, with center $\lambda_{\rm los}(x,y,z) = (1+V_{\rm los}(x,y,z)/c)\lambda_0$ and standard deviation $\sigma_\lambda = (\sigma_{V,0}/c)\lambda_0$. We thus expand our intensity cube into wavelength space as

$$I(x,y,z,\lambda) = \frac{I(x,y,z)}{\sigma_\lambda\sqrt{2\pi}}\exp\left[-\frac{(\lambda-\lambda_{\rm los}(x,y,z))^2}{2\sigma_\lambda^2}\right], \tag{A9}$$

where we normalize the intensity distribution to ensure $\int_\lambda I(x,y,z,\lambda)d\lambda = I(x,y,z)$.

We collapse the intensity over the z (line-of-sight) direction,

$$I(x,y,\lambda) = \int_{-\infty}^{+\infty} I(x,y,z,\lambda)dz, \tag{A10}$$

to estimate the observable spectral cube, which contains the combined line-of-sight velocity and velocity dispersion at every point (x,y).

The observed intensity is convolved with the atmospheric seeing. We model the PSF as a 2D gaussian and take the blurred intensity cube to be $I(x,y,\lambda)\otimes{\rm PSF}(x,y)$. The MOSFIRE spectra are taken through a slit, so there is only one dimension of spatial information. Thus we collapse the intensity model in the slit width axis, x, over the width of the slit, $x_{\rm ap}$ by taking

$$I(y,\lambda) = \int_{-x_{\rm ap}/2}^{+x_{\rm ap}/2}\left[I(x,y,\lambda)\otimes{\rm PSF}(x,y)\right]dx. \tag{A11}$$

Finally, we include the effects of instrumental resolution by convolving the model with a Gaussian with width $\sigma_{\lambda,\,\rm inst}$ (measured from the width of sky lines). An example Hα emission line model is shown in the right panel of Figure 20.

In practice, we generate a model by performing these calculation over a finite grid of values in x,y,z, and λ. We set $x_{\rm ap} = 0\farcs7$ (MOSFIRE slit width), and $y_{\rm ap}$ equal to the spatial extent of the trimmed 2D spectrum to which we will compare the model. We set $z_{\rm ap} = y_{\rm ap}$, to probe the same spatial extent both along the line-of-sight and along the slit. We allow for sub-pixel sampling, and set the number of sub-pixels in x,y,z so that the sub-pixel width in each dimension is nearly equal, while preserving an integer number of whole pixels in the spectrum spatial direction, y. Additionally, we pad the grid by $0.5\,{\rm FWHM}_{\rm seeing}$ arcsec on both sides in the x and y directions, to accurately calculate the seeing-convolved intensity over the full $x_{\rm ap}, y_{\rm ap}$. We sample the model at the wavelengths of the associated 2D spectrum in the range around Hα. The array $I(y,\lambda)$ is oversampled in the y direction. Finally, we re-bin the data to match the observed spatial pixel size by adding the sub-pixels in y. The final model $f_{\rm model}(y,\lambda)$ now samples the intensity at the exact spatial positions y and wavelengths λ covered by the data.

The resulting model of the observed kinematic signature of a disk galaxy depends on fixed parameters ΔPA, n, R_E, and b/a, all derived from the Sérsic fits performed using GALFIT. The seeing FWHM and instrument resolution are additional fixed parameters. Because we do not probe the flat part of the rotation curves for our galaxy sample, we fix y_0 and λ_0. We mask missing pixels and skylines for the 2D spectrum, collapse over λ and fix y_0 to the peak of a Gaussian fit. We similarly collapse over y to fit λ_0. The free parameters are V_a, r_t, and $\sigma_{V,0}$. V_a and r_t describe the arctan disk rotation model, while $\sigma_{V,0}$ introduces additional broadening in the wavelength direction.

Procedure for measuring kinematics from 2D emission lines

In this appendix we describe how we measure rotation and dispersion velocities from Hα emission lines that exhibit resolved rotation. For each object, we start by subtracting out the continuum from the Hα 2D spectrum. First, we measure the continuum slope of the optimally extracted 1D spectrum using a noise-weighted linear fit in the wavelength range $6454.6\text{Å} \le \lambda/(1+z_{\rm MOS}) \le 6674.6\text{Å}$, where we mask the H$\alpha$ and [NII] lines from $6533.6\text{Å} \le \lambda/(1+z_{\rm MOS}) \le 6599.6\text{Å}$. We then assume that the slope of the continuum in each spatial slice of the 2D spectrum is equal to the 1D continuum slope value, and perform a weighted linear fit in each spatial slice where only the intercept is allowed to vary. We subtract the best-fit continuum from each spatial slice to leave only the Hα line emission. Next, we trim the continuum-subtracted emission line 2D spectrum to the wavelength range $6555.6\text{Å} \le \lambda/(1+z_{\rm MOS}) \le 6573.6\text{Å}$, to exclude the [NII] emission lines from our resolved line fitting. As we exclude objects with outflows or AGN with very broad emission lines, [NII] contamination within this trimmed range should be minimal. We also trim the spectrum in the spatial direction so that only the positive emission line is retained.

To ensure that the model comparisons include only high S/N portions of each spectrum, we construct a mask $m(x,y)$, where x is the wavelength dispersion direction of the spectrum and y is the spatial direction. First, we mask pixels with missing data. Second, we mask rows where ${\rm S/N}(y) < 2$, leaving only contiguous rows with high S/N unmasked. The row S/N is estimated to be the total row flux over the total row error, with the pixel errors added in quadrature. We mask pixels with missing data or columns affected by skyline contamination in this S/N measurement. The columns affected by skyline contamination are identified as those where the total column error, added in quadrature, is 2 and 3 times greater than the median error of all columns in the spectrum, for the K and H bands, respectively.[3] We do not mask pixels affected by skyline contamination when fitting the models to the data, as these pixels are down-weighted in the fitting procedure because of their large errors relative to the non-contaminated pixels.

To find the best-fit model to the data, we first match the model intensity to the data intensity profile. We perform a weighted least squares fit of the model $f_{\rm model}(x,y)$ to the data $f(x,y)$ (with errors $\sigma_f(x,y)$) at each y and measure the appropriate scaling $S(y)$ between the model and data spatial rows

$$S(y) = \frac{\sum_x m(x,y)\left[f(x,y)f_{\rm model}(x,y)/\sigma_f(x,y)^2\right]}{\sum_x m(x,y)\left[f_{\rm model}(x,y)^2/\sigma_f(x,y)^2\right]}, \tag{A12}$$

where we mask missing data and columns contaminated by skyline emission with $m(x,y)$ (discussed in Section 3.1). We do not fix the scaling to the convolved and integrated (in the slit direction) GALFIT profile, as the line emission may be distributed differently (see Nelson et al. 2012). Nonetheless, in

[3] The sky background in the K band is higher than in H, so we adopt a less conservative skyline identification criterion for the K band.

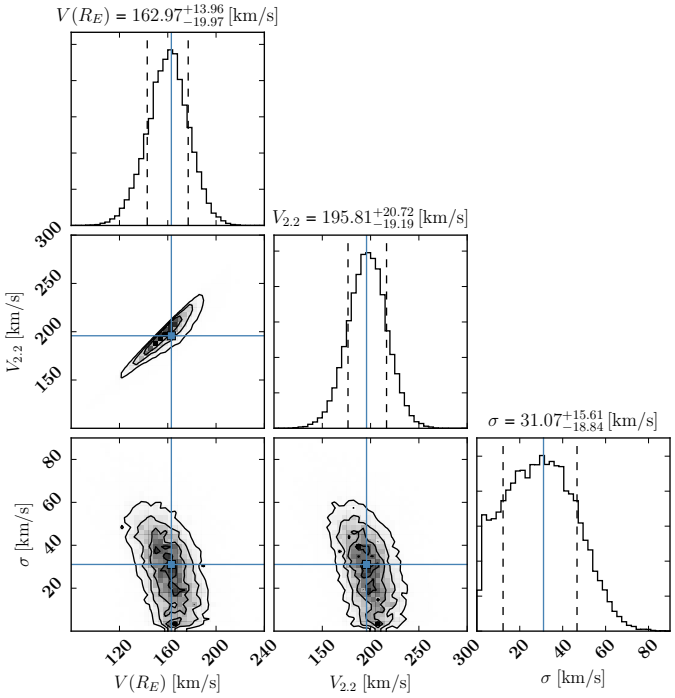

FIG. 21.— Example posterior distribution for $V(R_E)$, $V_{2.2}$, and $\sigma_{V,0}$ for COSMOS-13701 (the second galaxy shown in Figures 2 and 16). The best-fit value of each parameter is taken to be the peak of the respective marginalized posterior distributions, and are shown as the blue lines in the histograms. The lower and upper 68% confidence intervals on each parameter are shown as the dashed black lines. The best-fit values are also shown as blue lines and blue squares in the various two-parameter posterior plots. Figure made using `corner.py` (Foreman-Mackey et al. 2014).

modeling the kinematics, we adopt a Sérsic stellar light profile to determine the intensity-weighted velocities. In Section 5.6, we show that most objects have similar stellar light and Hα profiles, and also discuss the implications for the modeling results when the Hα profile differs from the stellar light profile.

The goodness-of-fit of the model is determined using a weighted χ^2 value. We choose the following weighting scheme to up-weight lower S/N rows, so the information in the fainter parts of the rotation curve is not lost:

$$w_y = [\mathrm{S/N}(y)]^{-1}\,. \tag{A13}$$

The weighted goodness-of-fit criterion is then

$$\chi^2_{\mathrm{weighted}} = \sum_{x,y} w_y \left[m(x,y)\frac{f(x,y) - S(y) f_{\mathrm{model}}(x,y)}{\sigma_f(x,y)} \right]^2 \tag{A14}$$

where we mask missing data and low S/N rows with $m(x,y)$, and the spectrum is dispersed in the x direction.

We use the `python` MCMC package, `emcee` (Foreman-Mackey et al. 2013) to find the best-fit models and confidence intervals. We define flat priors $\log p(X)$ for each parameter X (V_a, r_t, $\sigma_{V,0}$), with bounds calculated based on the spatial and wavelength coverage of the trimmed 2D spectrum, yielding composite prior $\log p(V_a, r_t, \sigma_{V,0}) = \Sigma_{\{X=V_a,r_t,\sigma_{V,0}\}} \log p(X)$. The log posterior probability is taken to be

$$\log P(V_a, r_t, \sigma_{V,0}|\lambda, f) = \log \mathcal{L}(f|\lambda, V_a, r_t, \sigma_{V,0}) + \log p(V_a, r_t, \sigma_{V,0}) + \mathrm{const}, \tag{A15}$$

with log likelihood probability $\log \mathcal{L} = -0.5\chi^2_{\mathrm{weighted}}$.

The rotation curve turnover is not well constrained in our data, so there is a degeneracy in the values of V_a and r_t. However, the values of $V(R_E)$ and $V_{2.2} = V(2.2r_s)$ are much better constrained. Thus we calculate $V(R_E)$ and $V_{2.2}$ for each pair of (V_a, r_t) values in the posterior sampling, to determine the posterior distributions on $V(R_E)$ and $V_{2.2}$. We take the best-fit values of $V(R_E)$, $V_{2.2}$, and $\sigma_{V,0}$ to be the peaks of the respective marginalized posterior distributions, and calculate the confidence intervals using the lower and upper 68-percentile bounds of the posterior distributions (e.g., see Figure 21).

Position-velocity diagrams for galaxies with detected rotation

To demonstrate the agreement between the observed and modeled kinematics, we measure velocity as a function of position from both the observed and modeled 2D spectra for each of the 35 galaxies with detected rotation. For each unmasked, high S/N row (see Appendix A.2), we fit the flux $f(x,y)$ with a Gaussian and determine the central wavelength, $\lambda(y)$, constraining λ to fall within $\pm 1.25\,\mathrm{FWHM}_{\lambda,\,1\mathrm{D},\,\mathrm{obs}}$ of the fixed central wavelength λ_0 (see Appendix A.1). We then calculate $V_{\mathrm{obs}}(y)$ from $\lambda(y)$ and λ_0. We estimate the errors in $V_{\mathrm{obs}}(y)$ by creating 500 realizations in which we perturb the flux $f(x,y)$ by the errors $\sigma_f(x,y)$, and repeat the fitting procedure on each realization. Finally, we correct the observed velocities for inclination, yielding $V_{\mathrm{obs}}(y)/(\sin i)$. The velocity profiles are shown in Figure 22. The observed and model velocity profiles are in good agreement, suggesting that our modeling approach works well.

APPENDIX B: INCLINATION AND APERTURE CORRECTION FOR UNRESOLVED DISK GALAXIES

If a disk galaxy is too small, it will be spatially unresolved and its rotation will not be detected. Additionally, some of the kinematic information may be missing because of slit losses. Furthermore, as our 1D spectra are optimally extracted, the observed velocity profile will depend on the inclination angle and the angle between the slit and the major axis of the galaxy. In this appendix we estimate the correction between the intrinsic kinematics and the kinematics within the extracted aperture for galaxies without detected rotation, assuming that they are rotationally supported disk galaxies. We make models of disk galaxies that account for variable inclination angles and variable ΔPA and use these models to calculate the integrated RMS velocity within the slit. We follow the general method presented in Appendix B of van de Sande et al. (2013) to calculate the aperture correction for a given kinematic and brightness profile.

The kinematics of the disk galaxy model are defined in the same way as in Appendix A. The slit coordinate system relative to the intrinsic galaxy coordinates is defined following Equations A4, A5. We assume that the rotation can be described with the arctan model (Equation A6). As we have no spatial information, we must assume a radial profile for the rotation curve, that is determined entirely through turnover radius, r_t. Based on the findings of Miller et al. (2011), we set $r_t = 0.4\,r_s = 0.4(R_E/1.676)$. Following Equation A7, the

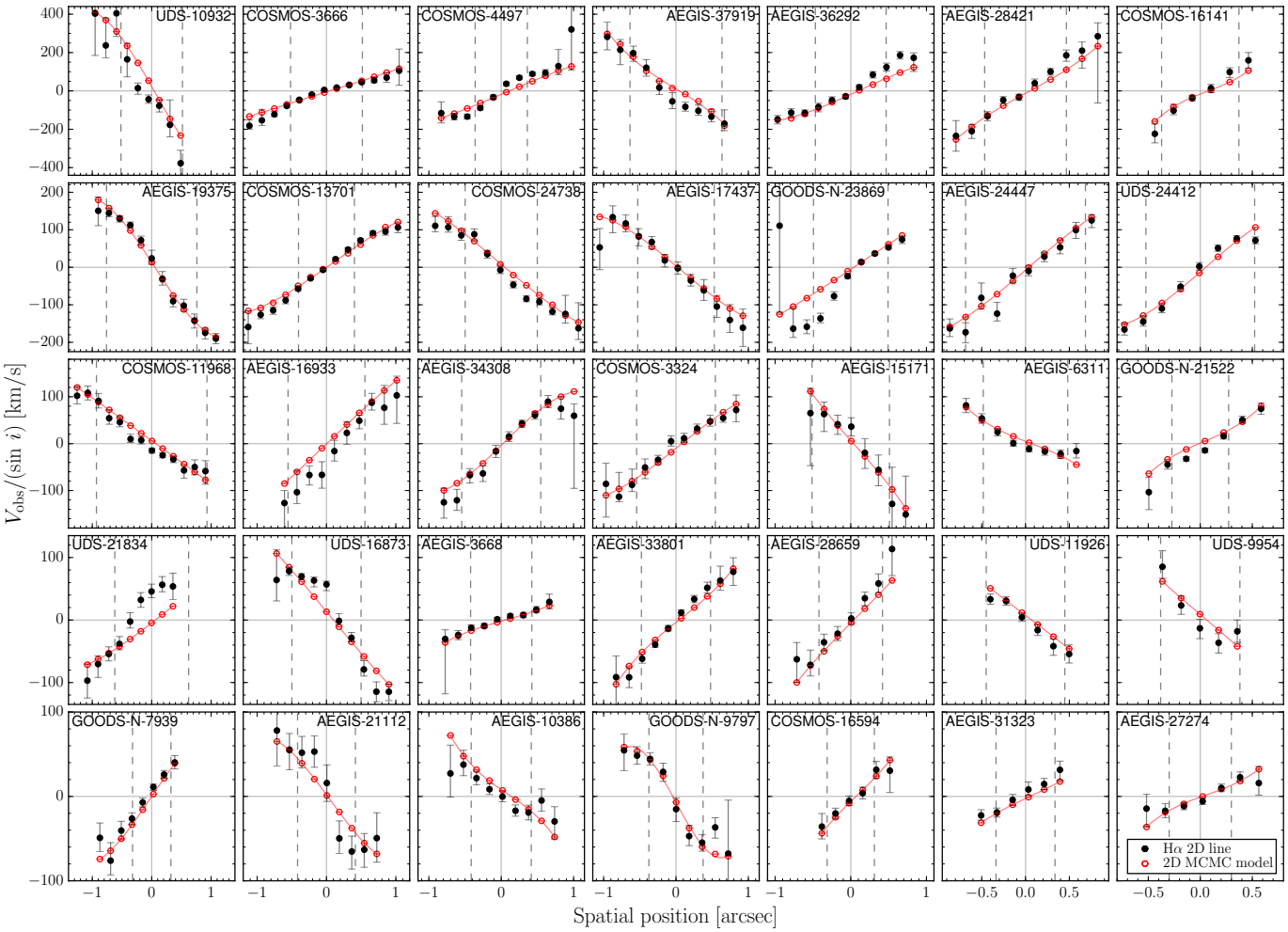

FIG. 22.— Position-velocity diagrams for the 35 MOSDEF galaxies with detected rotation. The velocity profile corrected for inclination $(V_{\rm obs}(y)/(\sin i)$; y axis) is measured versus the spatial position (x axis) from the 2D Hα emission line spectrum (black circles) and from the best-fit 2D line model (open red circles) for each object. The error bars do not include uncertainties from the inclination correction. For reference, we fit a third order polynomial (red line) to the model velocity profile. The vertical grey dashed lines show the projected effective radius convolved to match the MOSFIRE seeing. The velocity profiles of the observed and model spectra are in good agreement.

relative line-of-sight radial profile of the model rotation curve is then $V_{\rm los}(x,y,z)/V(R_E)$, in which we do not assume an absolute velocity scale. Since our galaxies may not be ideal disks, we assume a simple constant dispersion velocity $\sigma_{V,0}$ and a fixed value of $(V/\sigma_{V,0})_{R_E} = V(R_E)/\sigma_{V,0}$.

Following Cappellari (2008), we assume the observed velocity dispersion is the square root of the second velocity moment, i.e. the RMS velocity, $V^2_{\rm RMS} = \sigma^2 + V^2$. To obtain relative quantities, we divide both sides by $V(R_E)$:

$$\left(\frac{V_{\rm RMS,\,los}(x,y,z)}{V(R_E)}\right)^2 = \left(\frac{1}{(V/\sigma_{V,0})_{R_E}}\right)^2 + \left(\frac{V_{\rm los}(x,y,z)}{V(R_E)}\right)^2 \quad \text{(B1)}$$

The total observed velocity dispersion of a galaxy is the combination of the intensity-weighted velocity dispersions at every point of the galaxy, so we must also assume a light profile to include in our models. As in Appendix A, we assume a modified Sérsic intensity profile $I(r,n,R_E,z_{\rm int},\sigma_z)$ (Equation A8).

We calculate the intensity-weighted dispersion within the aperture from the RMS velocity relative to $V(R_E)$, following Equation B9 of van de Sande et al. (2013):

$$\left(\frac{\sigma_{V,\,\rm model}}{V(R_E)}\right)^2 = \quad \text{(B2)}$$
$$\frac{\sum_{-X}^{X}\sum_{-Y}^{Y}\left(\left[\sum_{-Z}^{Z}\left(\frac{V_{\rm RMS,los}(x,y,z)}{V(R_E)}\right)^2 I(x,y,z)\Delta z\right]\otimes {\rm PSF}\right) g(y)\Delta x\Delta y}{\sum_{-X}^{X}\sum_{-Y}^{Y}\left(\left[\sum_{-Z}^{Z} I(x,y,z)\Delta z\right]\otimes {\rm PSF}\right) g(y)\Delta x\Delta y}$$

Here we define $X = \frac{1}{2}x_{\rm ap}$, $Y = \frac{1}{2}y_{\rm ap}$, and $Z = \frac{1}{2}z_{\rm ap}$, and define $V_{\rm RMS,los}/V(R_E)$ from Equation B1. We model the PSF as a 2D Gaussian with FWHM equal to that atmospheric seeing FWHM, and adopt the same spatial weighting function $g(y)$ as used in extracting the MOSDEF 1D spectra.

The dynamical masses of disk galaxies are calculated using the velocity at a specific radius, i.e. $V(R_E)$, instead of an integrated velocity dispersion. Thus, instead of calculating σ_e, the intrinsic intensity-weighted velocity dispersion within the effective radius R_E, we calculate the RMS velocity of the model at $r = R_E$, $V_{\rm RMS}(R_E)_{\rm model} = \sqrt{\sigma^2_{V,0} + V(R_E)^2}$,

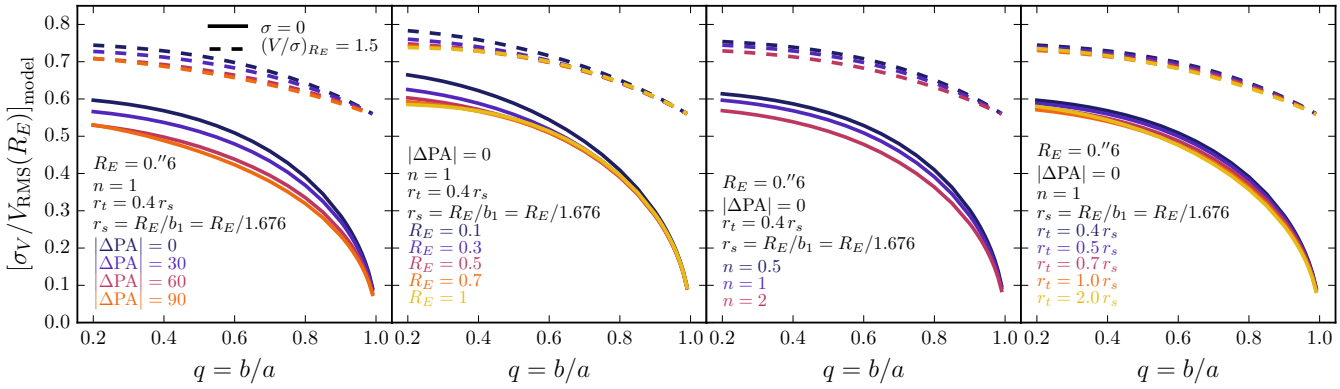

FIG. 23.— Aperture corrections, $\sigma_{V,\,\rm model}/V_{\rm RMS}(R_E)_{\rm model}$, for disk galaxies without resolved rotation, as a function of (a) ΔPA, (b) R_E, (c) n, and (d) r_t. We show the aperture correction assuming no intrinsic velocity dispersion ($\sigma_{V,0} = 0$, solid lines) and partial rotational support ($(V/\sigma_{V,0})_{R_E} = 1.5$, dashed lines). The non-variable parameters in each panel are set to $\Delta{\rm PA} = 0$, $R_E = 0.''6$, $n = 1$, and $r_t = 0.4r_s = 0.4(R_E/1.676)$. We assume a seeing FWHM of $0.''6$ for every model.

relative to $V(R_E)$, which we write as:

$$\frac{V_{\rm RMS}(R_E)_{\rm model}}{V(R_E)} = \sqrt{1 + \frac{1}{(V/\sigma_{V,0})^2_{R_E}}}. \quad \text{(B3)}$$

The observed velocity dispersion corrected for both aperture and inclination effects, and converted to a RMS velocity, is the combination of Equations B2 and B3:

$$V_{\rm RMS}(R_E)_{\rm corr} = \sigma_{\rm obs} \left(\frac{\sigma_{V,\,\rm model}}{V_{\rm RMS}(R_E)_{\rm model}} \right)^{-1}, \quad \text{(B4)}$$

with

$$\frac{\sigma_{V,\,\rm model}}{V_{\rm RMS}(R_E)_{\rm model}} = \left(\frac{\sigma_{V,\,\rm model}}{V(R_E)} \right) \frac{(V/\sigma_{V,0})_{R_E}}{\sqrt{1 + (V/\sigma_{V,0})^2_{R_E}}}. \quad \text{(B5)}$$

To calculate the correction $\sigma_{V,\,\rm model}/V_{\rm RMS}(R_E)_{\rm model}$ for individual galaxies, we use the best-fit GALFIT parameters for n, $R_E = a$ (the semi-major axis), and $q = b/a$. We set $x_{\rm ap} = 0.''7$, the slit width for all observations, and set $y_{\rm ap} = y_{\rm extract}$, the actual width used to extract the 1D spectra. We choose $z_{\rm ap} = y_{\rm ap}$, to probe the same spatial extent in the line-of-sight direction as we probe along the slit.

In practice, we initially pad coordinate grids in the x, y directions by $0.5\,{\rm FWHM}_{\rm seeing}$ arcsec, to accurately consider the convolution with the atmospheric seeing across the aperture edges. We include these pixels when calculating the collapse over z and the convolution with the seeing, then remove the padded pixels for the final sum within the aperture. We sample the model over a large number of pixels, and choose the pixel sizes so they are nearly equal in all dimensions, $\Delta y = \Delta z \approx \Delta x$, with the constraint that there must be an integer number of pixels within $x_{\rm ap}$ and $y_{\rm ap}$.

The effects of varying the model parameters b/a, ΔPA, R_E, n, and r_t are demonstrated in Figure 23. In all cases, we assume a typical seeing of $0.''6$. We adopt $x_{\rm ap} = 0.''7$, the slit width for all MOSDEF observations, and set $y_{\rm ap} = 4R_{E,\,\rm proj+conv}$, to approximate dependance of aperture size on the object size, misalignment, and seeing that is incorporated in the data extraction method.

The inclination angle has the largest influence on the correction value. At a fixed axis ratio, the inclusion of a finite $(V/\sigma_{V,0})_{R_E}$ value causes the largest difference in the aperture correction, as the intrinsic velocity dispersion increases the observed LOS velocity dispersion. The position angle offset causes larger variations for more edge-on disks ($b/a \approx (b/a)_0$) than for disks closer to face-on ($b/a \approx 1$), as the more face-on disks are much closer to being round, and the amount of the disk falling outside of the slit for any ΔPA is similar. Variations with the Sérsic index n reflect how the different intensity profiles weight the velocity distribution. Changes of the assumed r_t affect the rotational velocity profile, with larger r_t moving the velocity turnover to larger radii. When combined with the Sérsic intensity weighting, this leads to smaller integrated velocity values. Finally, when the disk is aligned with the major axis, the aperture correction varies little with the effective radius R_E. The aperture correction varies more with R_E when combined with larger ΔPA offsets.

REFERENCES

Bell, E. F., & de Jong, R. S. 2001, ApJ, 550, 212
Belli, S., Newman, A. B., & Ellis, R. S. 2014, ApJ, 783, 117
Bezanson, R., Franx, M., & van Dokkum, P. G. 2015, ApJ, 799, 148
Bezanson, R., van Dokkum, P., van de Sande, J., Franx, M., & Kriek, M. 2013, ApJ, 764, L8
Blanton, M. R., & Moustakas, J. 2009, ARA&A, 47, 159
Blumenthal, G. R., Faber, S. M., Primack, J. R., & Rees, M. J. 1984, Nature, 311, 517
Bouché, N., Cresci, G., Davies, R., et al. 2007, ApJ, 671, 303
Bournaud, F., Chapon, D., Teyssier, R., et al. 2011, ApJ, 730, 4
Brammer, G. B., van Dokkum, P. G., Franx, M., et al. 2012, ApJS, 200, 13
Brewer, B. J., Dutton, A. A., Treu, T., et al. 2012, MNRAS, 422, 3574
Buitrago, F., Conselice, C. J., Epinat, B., et al. 2014, MNRAS, 439, 1494
Cacciato, M., Dekel, A., & Genel, S. 2012, MNRAS, 421, 818
Calzetti, D., Armus, L., Bohlin, R. C., et al. 2000, ApJ, 533, 682
Cappellari, M. 2008, MNRAS, 390, 71
Cappellari, M., Bacon, R., Bureau, M., et al. 2006, MNRAS, 366, 1126
Cardelli, J. A., Clayton, G. C., & Mathis, J. S. 1989, ApJ, 345, 245
Ceverino, D., Dekel, A., Mandelker, N., et al. 2012, MNRAS, 420, 3490
Chabrier, G. 2003, PASP, 115, 763
Chapman, S. C., Blain, A. W., Smail, I., & Ivison, R. J. 2005, ApJ, 622, 772
Ciotti, L., & Bertin, G. 1999, A&A, 352, 447
Coil, A. L., Aird, J., Reddy, N., et al. 2015, ApJ, 801, 35
Conroy, C., & Gunn, J. E. 2010, ApJ, 712, 833
Conroy, C., Gunn, J. E., & White, M. 2009, ApJ, 699, 486
Contini, T., Garilli, B., Le Fèvre, O., et al. 2012, A&A, 539, A91
Courteau, S. 1997, AJ, 114, 2402
Daddi, E., Dannerbauer, H., Elbaz, D., et al. 2008, ApJ, 673, L21

Daddi, E., Bournaud, F., Walter, F., et al. 2010, ApJ, 713, 686
Dalcanton, J. J., Spergel, D. N., & Summers, F. J. 1997, ApJ, 482, 659
Davé, R. 2008, MNRAS, 385, 147
Dekel, A., & Birnboim, Y. 2006, MNRAS, 368, 2
Dekel, A., Sari, R., & Ceverino, D. 2009, ApJ, 703, 785
Dutton, A. A. 2009, MNRAS, 396, 121
Dutton, A. A., Conroy, C., van den Bosch, F. C., et al. 2011a, MNRAS, 345, 322
Dutton, A. A., van den Bosch, F. C., Faber, S. M., et al. 2011b, MNRAS, 410, 1660
Elmegreen, B. G., & Elmegreen, D. M. 2006, ApJ, 650, 644
Elmegreen, D. M., Elmegreen, B. G., Marcus, M. T., et al. 2009, ApJ, 701, 306
Elmegreen, D. M., Elmegreen, B. G., Ravindranath, S., & Coe, D. a. 2007, ApJ, 658, 763
Epinat, B., Amram, P., Balkowski, C., & Marcelin, M. 2010, MNRAS, 401, 2113
Epinat, B., Amram, P., Marcelin, M., et al. 2008, MNRAS, 388, 500
Epinat, B., Contini, T., Le Fèvre, O., et al. 2009, A&A, 504, 789
Epinat, B., Tasca, L., Amram, P., et al. 2012, A&A, 539, A92
Erb, D. K., Steidel, C. C., Shapley, A. E., et al. 2006, ApJ, 646, 107
Fall, S. M., & Efstathiou, G. 1980, MNRAS, 193, 189
Fan, X., Strauss, M. A., Schneider, D. P., et al. 2001, AJ, 121, 54
Foreman-Mackey, D., Hogg, D. W., Lang, D., & Goodman, J. 2013, PASP, 125, 306
Foreman-Mackey, D., Price-Whelan, A., Ryan, G., et al. 2014, corner.py v0.1.1, Zenodo, doi:10.5281/zenodo.11020
Förster Schreiber, N. M., Genzel, R., Lehnert, M. D., et al. 2006, ApJ, 645, 17
Förster Schreiber, N. M., Genzel, R., Bouché, N., et al. 2009, ApJ, 706, 1364
Förster Schreiber, N. M., Genzel, R., Newman, S. F., et al. 2014, ApJ, 787, 38
Freeman, K. C. 1970, ApJ, 160, 811
Gabor, J. M., & Bournaud, F. 2014, MNRAS, 441, 1615
Genel, S., Dekel, A., & Cacciato, M. 2012, MNRAS, 425, 788
Genzel, R., Burkert, A., Bouché, N., et al. 2008, ApJ, 687, 59
Genzel, R., Tacconi, L. J., Gracia-Carpio, J., et al. 2010, MNRAS, 407, 2091
Genzel, R., Newman, S., Jones, T., et al. 2011, ApJ, 733, 101
Genzel, R., Förster Schreiber, N. M., Lang, P., et al. 2014, ApJ, 785, 75
Genzel, R., Tacconi, L. J., Lutz, D., et al. 2015, ApJ, 800, 20
Gnerucci, A., Marconi, A., Cresci, G., et al. 2011, A&A, 528, A88
Governato, F., Willman, B., Mayer, L., et al. 2007, MNRAS, 374, 1479
Green, A. W., Glazebrook, K., McGregor, P. J., et al. 2014, MNRAS, 437, 1070
Grogin, N. A., Kocevski, D. D., Faber, S. M., et al. 2011, ApJS, 197, 35
Hopkins, A. M., & Beacom, J. F. 2006, ApJ, 651, 142
Kassin, S. A., Weiner, B. J., Faber, S. M., et al. 2007, ApJ, 660, L35
—. 2012, ApJ, 758, 106
Kennicutt, R. C. 1998, ApJ, 498, 541
Kereš, D., Katz, N., Fardal, M., Davé, R., & Weinberg, D. H. 2009, MNRAS, 395, 160
Kereš, D., Katz, N., Weinberg, D. H., & Dave, R. 2005, MNRAS, 363, 2
Koekemoer, A. M., Faber, S. M., Ferguson, H. C., et al. 2011, ApJS, 197, 36
Kriek, M., van Dokkum, P. G., Labbé, I., et al. 2009, ApJ, 700, 221
Kriek, M., Shapley, A. E., Reddy, N. A., et al. 2015, ApJS, 218, 15
Law, D. R., Steidel, C. C., Erb, D. K., et al. 2007a, ApJ, 669, 929
—. 2009, ApJ, 697, 2057
—. 2007b, ApJ, 656, 1
Law, D. R., Steidel, C. C., Shapley, A. E., et al. 2012a, ApJ, 759, 29
—. 2012b, ApJ, 745, 85
McLean, I. S., Steidel, C. C., Epps, H., et al. 2010, in Proceedings of SPIE, ed. I. S. McLean, S. K. Ramsay, & H. Takami, Vol. 7735, 77351E–77351E–12
McLean, I. S., Steidel, C. C., Epps, H. W., et al. 2012, in Proceedings of SPIE, ed. I. S. McLean, S. K. Ramsay, & H. Takami, Vol. 8446, 84460J
Meurer, G. R., Carignan, C., Beaulieu, S. F., & Freeman, K. C. 1996, AJ, 111, 1551
Miller, S. H., Bundy, K., Sullivan, M., Ellis, R. S., & Treu, T. 2011, ApJ, 741, 115
Miller, S. H., Ellis, R. S., Sullivan, M., et al. 2012, ApJ, 753, 74
Miller, S. H., Sullivan, M., & Ellis, R. S. 2013, ApJ, 762, L11
Mo, H. J., Mao, S., & White, S. D. M. 1998, MNRAS, 295, 319
Momcheva, I. G., Brammer, G. B., van Dokkum, P. G., et al. 2015, submitted to ApJSS, arXiv: 1510.02106
Nelson, E. J., van Dokkum, P. G., Brammer, G., et al. 2012, ApJ, 747, L28
Nelson, E. J., van Dokkum, P. G., Momcheva, I., et al. 2013, ApJ, 763, L16
Nelson, E. J., van Dokkum, P. G., Schreiber, N. M. F., et al. 2015, submitted to ApJ, arXiv: 1507.03999
Newman, A. B., Ellis, R. S., Treu, T., & Bundy, K. 2010, ApJ, 717, L103
Newman, S. F., Genzel, R., Förster Schreiber, N. M., et al. 2013, ApJ, 767, 104
Noeske, K. G., Weiner, B. J., Faber, S. M., et al. 2007, ApJ, 660, L43
Oser, L., Ostriker, J. P., Naab, T., Johansson, P. H., & Burkert, A. 2010, ApJ, 725, 2312
Osterbrock, D. E., & Ferland, G. J. 2006, Astrophysics of gaseous nebulae and active galactic nuclei, 2nd edn. (Sausalito, CA: University Science Books)
Peng, C. Y., Ho, L. C., Impey, C. D., & Rix, H.-W. 2010, AJ, 139, 2097
Pettini, M., Shapley, A. E., Steidel, C. C., et al. 2001, ApJ, 554, 981
Pizagno, J., Prada, F., Weinberg, D. H., et al. 2005, ApJ, 633, 844
Price, S. H., Kriek, M., Brammer, G. B., et al. 2014, ApJ, 788, 86
Reddy, N. A., & Steidel, C. C. 2009, ApJ, 692, 778
Reddy, N. A., Kriek, M., Shapley, A. E., et al. 2015, ApJ, 806, 259
Salpeter, E. E. 1955, ApJ, 121, 161
Sérsic, J. L. 1968, Atlas de galaxias australes (Cordoba, Argentina: Observatorio Astronomico)
Sharples, R., Bender, R., Agudo Berbel, A., et al. 2013, The Messenger, 151, 21
Sharples, R. M., Bender, R., Lehnert, M. D., et al. 2004, in Proceedings of SPIE, ed. A. F. M. Moorwood & M. Iye, Vol. 5492, 1179–1186
Shivaei, I., Reddy, N. A., Shapley, A. E., et al. 2015, accepted to ApJ, arXiv: 1507.03017
Simard, L., & Pritchet, C. J. 1999, PASP, 111, 453
Skelton, R. E., Whitaker, K. E., Momcheva, I. G., et al. 2014, ApJS, 214, 24
Swinbank, A. M., Papadopoulos, P. P., Cox, P., et al. 2011, ApJ, 742, 11
Szomoru, D., Franx, M., Bouwens, R. J., et al. 2011, ApJ, 735, L22
Szomoru, D., Franx, M., van Dokkum, P. G., et al. 2013, ApJ, 763, 73
Tacconi, L. J., Genzel, R., Smail, I., et al. 2008, ApJ, 680, 246
Tacconi, L. J., Genzel, R., Neri, R., et al. 2010, Nature, 463, 781
Tacconi, L. J., Neri, R., Genzel, R., et al. 2013, ApJ, 768, 74
Taylor, E. N., Franx, M., Brinchmann, J., van der Wel, A., & van Dokkum, P. G. 2010, ApJ, 722, 1
Tully, R. B., & Fisher, J. R. 1977, A&A, 54, 661
van de Sande, J., Kriek, M., Franx, M., et al. 2013, ApJ, 771, 85
van den Bosch, F. C. 2001, MNRAS, 327, 1334
van der Wel, A., Franx, M., van Dokkum, P. G., et al. 2014a, ApJ, 788, 28
van der Wel, A., Chang, Y.-Y., Bell, E. F., et al. 2014b, ApJ, 792, L6
van Dokkum, P. G., Leja, J., Nelson, E. J., et al. 2013, ApJ, 771, L35
van Dokkum, P. G., Nelson, E. J., Franx, M., et al. 2015, ApJ, 813, 23
Vergani, D., Epinat, B., Contini, T., et al. 2012, A&A, 546, A118
Vogt, N. P., Forbes, D. A., Phillips, A. C., et al. 1996, ApJ, 465, L15
Weiner, B. J., Willmer, C. N. A., Faber, S. M., et al. 2006, ApJ, 653, 1049
White, S. D. M., & Frenk, C. S. 1991, ApJ, 379, 52
White, S. D. M., & Rees, M. J. 1978, MNRAS, 183, 341
Williams, R. J., Quadri, R. F., Franx, M., van Dokkum, P., & Labbé, I. 2009, ApJ, 691, 1879
Williams, R. J., Quadri, R. F., Franx, M., et al. 2010, ApJ, 713, 738
Wisnioski, E., Glazebrook, K., Blake, C., et al. 2012, MNRAS, 422, 3339
Wisnioski, E., Förster Schreiber, N. M., Wuyts, S., et al. 2015, ApJ, 799, 209
Wright, S. A., Larkin, J. E., Law, D. R., et al. 2009, ApJ, 699, 421
Wright, S. A., Larkin, J. E., Barczys, M., et al. 2007, ApJ, 658, 78
Wuyts, S., Labbe, I., Franx, M., et al. 2007, ApJ, 655, 51